Title
Collective Dynamics of Rigid Disks on a Non-Newtonian Membrane

Author
VIG, VISHNU

Publication Date
2021

Peer reviewed|Thesis/dissertation

Collective Dynamics of Rigid Disks on a Non-Newtonian Membrane

By

VISHNU VIG
THESIS

Submitted in partial satisfaction of the requirements for the degree of

MASTER OF SCIENCE

in

CHEMICAL ENGINEERING

in the

OFFICE OF GRADUATE STUDIES

of the

UNIVERSITY OF CALIFORNIA

DAVIS

Approved:

Harishankar Manikantan

Ronald J. Phillips

Greg Miller

Committee in Charge

2021

I would like to dedicate this work to my family for their continuous support throughout my journey. Grandpa, Its a few months since you passed away, but I've honored your last words and completed this work. I wish you could be there at my graduation. We all miss you.

Contents

Abstract

Biological membranes are made of phospholipids and host numerous surface active components. They are ubiquitous in nature and exhibit a non-trivial rheology, where the surface shear viscosity of an insoluble monolayer often depends on its surface-pressure. In this work, we extend the current Newtonian framework to account for this non-Newtonian behavior and unravel its effect on particles translating under low-Reynolds number hydrodynamics. We use a perturbative approach to model a weakly non-Newtonian membrane and compute its leading order effect on rigid disks by employing the Lorentz Reciprocal theorem. In particular, we show that a rigid disk translating on a free-standing membrane with background shear, experiences a force due to membrane rheology and undergoes non-intuitive trajectories, similar to the Saffman-lift force on spheres. We explored the effect of this force on the collective dynamics of rigid disks by simulating the uniform translation of multiple rigid disks on a membrane. We report the formation of disk aggregates with a hexatic order that is found to be sensitive to the surface pressure-viscosity dependence.

Acknowledgments

I'd like to thank my major professor, Dr. Harishankar Manikantan for his invaluable guidance, patience and support during my Masters study. This work would not have been possible without your insight and encouragement. My gratitude extends to my theses committee: Dr. Ronald J. Phillips and Dr. Greg Miller, for reviewing my work and for being great educators. I am lucky to have attended your classes and your course notes have helped me countless times throughout this theses. I am grateful to Ms. Grace Woods, Mr. Wallace Woods and Mr. Ryan Gorsiski for guiding me efficiently through administrative procedures during the COVID pandemic.

I am indebted to UC Davis Chemical Engineering Department for providing a nurturing experience and am proud to submit this work as an Aggie. Finally, I'd like to thank my housemates' cats Nala and Newton for being the ultimate stress buster. I thoroughly enjoyed making you chase a shoe string and will miss having you walk on my laptop during zoom meetings.

CHAPTER 1

Introduction

Fluid-fluid interfaces are present just about everywhere, in nature and in industry. They are formed when the intra-molecular forces within the fluids are more attractive than entropic effects and the inter-molecular forces between them; such that the enthalpic interactions between particles dictate the thermodynamics of mixing and favour the formation of a 'separate phase' [**1**]. When both the fluids are simple, they form a 'clean' interface characterized by their interfacial surface tension (e.g. air bubbles in water, immiscible liquids etc.) [**2**]. However, interfaces may also contain surfactants, trans-membrane proteins, macro-molecules or artificially engineered micro/nano-sized particles that reduce its surface tension by lowering the interfacial area and introduce phenomena like Marangoni flows [**3**, **4**] and surface rheology [**5**, **6**]. Such complex interfaces are a significant part of various biological and manufacturing processes. They are prevalent in foams and emulsions [**7**–**10**]; in bio-processes like cell transduction and cell division [**11**–**14**]; in consumer products and food science [**15**]; in solid-stabilized Pickering-Ramsden emulsions [**16**, **17**].

In recent years, the complex fluid interface in biological systems has been a topic of interest for chemical engineers, where a vast range of problems relate the membrane dynamics to its constitutive structural components. Membranes of living cells are formed from phospholipid bilayers [**18**] and host numerous proteins/surfactants that carry out important cellular functions like transfer of oxygen from our lungs to blood stream [**19**], maintaining cellular metabolic activity [**20**] and transduction of signals via receptors for immune response [**21**, **22**]. Researchers have also been studying biofilm-based approaches in wound management/cellular repair by using surfactants [**23**]. Living microorganisms like bacteria and fungi secrete surface-active molecules atop a biofilm that induce surface concentration gradient driven flows and affect their swarming motility [**24**, **25**]. Certain bacteria have also been found to use the Marangoni phenomena in expanding their colonies on a biofilm by 'surfing on waves of surfactants' [**26**]. The fact that complex interfaces play a significant part in such diverse fields of science, makes the study of their underlying dynamics highly relevant.

Biological membranes are a class of complex interfaces with a rich variety of physio-chemical transport phenomena. Several models (Fig. 1.1) have been used in explaining the structural and dynamical aspects of biological membranes. The fluid mosaic model from 1972 [**27**] had a strong influence on the interpretation of membrane dynamics and suggested that lipid bilayers form a two-dimensional matrix, hosting proteins and other surface active particles that carry out the respective biological functions of the membrane. The two-dimensional lipid matrix has inherent fluidity and restricted lateral diffusion. It was also assumed here that the membrane inclusions were randomly distributed, thereby neglecting any lateral heterogeneity along the membrane. However, subsequent developments in microscopy techniques led to publications that countered the assumptions in the fluid mosaic model and supported membrane heterogeneity and formation of functional membrane domains [**28**–**30**]. The next major framework describing a biological membrane was the raft hypothesis from 1997 [**31**]. In this model, membranes are assumed to contain cholesterol, glycosphingolipids and protein receptors organized in glycolipoprotein domains called lipid rafts. These protein-lipid microdomains carry out specific biological functions and float freely within the membrane bilayer. There has been evidence supporting [**32**–**35**] and opposing [**36**, **37**] this hypothesis and since these rafts have not been observed directly due to limited resolution in modern microscopic techniques, the validity of this hypothesis remains questionable [**38**].

A continuum level approach in analysing complex interfaces like phospholipid membranes, involves a macroscopic perspective that omits molecular details of the interface and assumes a continuous distribution of matter in the system. This involves treating the interface as a thin layer of viscous fluid and modelling the proteins/surfactants as inclusions embedded in this layer of fluid. Numerous publications have made use of the continuum perspective to explain dynamics behind complex interfacial phenomena like the lateral diffusion of membrane proteins in a biological membrane [**41**], the anomalous settling of surfactant covered drops [**42**], the coffee ring effect [**43**], the Saffman-Taylor instability in surfactant-laden interfaces [**44**] etc. In this work, we employ the continuum mechanics approach in modeling a membrane with surface-pressure dependent rheology and unravel the effect of its rheology on the collective behavior of surface-passive particles (modelled as rigid disks) translating uniformly on the interface. The following sections (§1.1-§1.4) discuss the development and mathematics of the continuum approach and §1.5 introduces the non-Newtonian

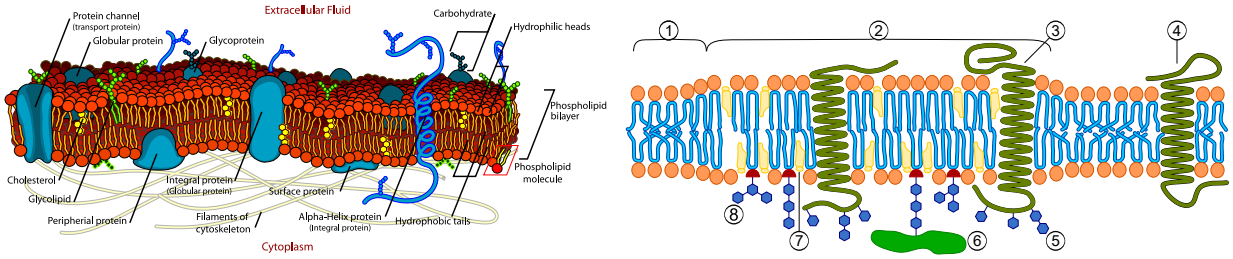

(a) Fluid mosaic model [**39**] (b) Lipid raft model [**40**]

FIGURE 1.1. (a) The fluid mosaic model describes a biological membrane as a two-dimensional lipid matrix of randomly distributed proteins that carry out specific biological functions. The model outlines the membrane as a fluid and suggests homogeneity along the bilayer. (b) Lipid raft model supports heterogeneity along the membrane and assumes the existence of functional protein-lipid microdomains that perform biological operations and float freely along the lipid bilayer. The numbered parts represent: 1. Non-raft membrane 2. Lipid raft 3. Lipid raft associated transmembrane protein 4. Non raft membrane protein 5. Glycosylation modifications (on glycoproteins and glycolipids) 6. GPI-anchored protein 7. Cholesterol 8. Glycolipid.

rheology of the interface in our problem. In chapter §2, we translate the Newtonian model for interfaces to account for a weakly non-Newtonian rheology and explore its effect on a rigid inclusion translating with a background shear on the membrane. In chapter §3, we elucidate the methods used in continuum simulation of multiple rigid inclusions translating on our non-Newtonian membrane and discuss the corresponding results in chapter §4. Finally, we close with concluding remarks and briefly explore improvements / applications of our study in chapter §5.

1.1. Two-Dimensional Hydrodynamics

The Knudsen number is the ratio of molecular mean free path of a system to its characteristic length scale. It helps in determining whether an atomistic or a continuum formulation should be used to model the dynamics of a system. An order of magnitude analysis confirms the ability of continuum mechanics to model the dynamics of micron sized inclusions atop interfaces and biomembranes, as the mean free path in such configurations measures only a few nanometers long [**45**]. This observation leads us to the two-dimensional fluid dynamic description of an interface.

The field of 2D hydrodynamics is complicated as motion of a surfactant on an interfaces simultaneously introduces multiple surface phenomena such as surfactant adsorption/desorption, Marangoni flows and surface diffusion. These phenomena relax interfacial stresses by redistributing surfactants.

Further, surfactants also exhibit surface rheology and exert additional stresses upon interfacial deformation. Surface rheology has been an active subject of study since the 1900s. Boussinesq (1913) explained the abnormal settling of a spherical drop in an unbounded fluid using surface-excess viscosity of the bubble, causing it to dissipate energy as it deforms [**42**]. Scriven (1960) extended Boussinesq's analysis and described an interface as a 2D Newtonian fluid with surface dilatational (κ_s) and surface shear (η_s) viscosities and developed governing equations describing the conservation of momentum at fluid-fluid interfaces [**46**]. This framework has now been established through decades of experimental, theoretical and computational studies and is well known as the Boussinesq-Scriven Model.

1.2. The Boussinnesq-Scriven Model

The model considers an interfacial layer as a 2D Newtonian fluid with inherent surface shear (η_s) and surface dilatiational (κ_s) viscosities. The resulting surface-stress tensor comprises of isotropic surface-pressure (surface tension) and the excess surface-rheological stresses [**46**].

$$\boldsymbol{\sigma}_s = -\Pi \mathbf{I}_s + \boldsymbol{\tau}_{\text{rheo}}, \tag{1.1}$$

$$\boldsymbol{\tau}_{\text{rheo}} = \left[(\kappa_s - \eta_s)\boldsymbol{\nabla}_s \cdot \mathbf{u}_s\right]\mathbf{I}_s + \eta_s\left[\boldsymbol{\nabla}_s\mathbf{u}\cdot\mathbf{I}_s + \mathbf{I}_s\cdot(\boldsymbol{\nabla}_s u)^{\mathrm{T}}\right]. \tag{1.2}$$

Here, $\mathbf{I}_s = \mathbf{I} - \mathbf{nn}$ is the surface identity tensor, $\mathbf{u}_s$ is the surface velocity, Π is the surface pressure and $\boldsymbol{\nabla}_s = \mathbf{I}_s \cdot \boldsymbol{\nabla}$ is the surface gradient tensor. This is much like the classic formulation of a 3D Newtonian fluid, with the subtlety of 2D viscosities having dimensions of 3D viscosity $\times$ length. Applying the 2D Cauchy momentum equation to a planar interface at the x-y plane gives [**47**]:

$$\rho_s \frac{D\mathbf{u}_s}{Dt} = \boldsymbol{\nabla}_s \cdot \boldsymbol{\sigma}_s - \eta \left.\frac{\partial \mathbf{v}}{\partial z}\right|_{\text{z=0}}, \tag{1.3}$$

where η is the 3D viscosity of the subphase, $\mathbf{v}$ is the subphase velocity and $\eta\,\partial\mathbf{v}/\partial z|_{z=0}$ is the viscous traction from the subphase on the interface. Viscous traction couples the interfacial and the subphase hydrodynamics by acting as a boundary condition (Eq. 1.3) in the subphase stress balance. Alternatively, we may think of viscous traction as a body force (that arises from the surrounding fluid) in the stress balance on the interface.

Neglecting fluid and surfactant inertia for quiescent flows on a planar interface, (Eq. 1.3) becomes:

$$\eta \frac{\partial \mathbf{v}}{\partial z}\bigg|_{\mathrm{z=0}} = -\boldsymbol{\nabla}_s \Pi + \boldsymbol{\nabla}_s \cdot \boldsymbol{\tau}_{\mathrm{rheo}}, \tag{1.4}$$

which can be simplified further to give:

$$\eta \frac{\partial \mathbf{v}}{\partial z}\bigg|_{\mathrm{z=0}} = -\boldsymbol{\nabla}_s \Pi + \eta_s \boldsymbol{\nabla}_s^2 \mathbf{u}_s + \kappa_s \boldsymbol{\nabla}_s (\boldsymbol{\nabla}_s \cdot \mathbf{u}_s). \tag{1.5}$$

Motion of an inclusion on a surfactant-laden interface compresses/dilates the interface along/against its direction of motion and establishes a surface concentration gradient around itself (Fig. 1.2). An insoluble interface balances these gradients predominantly by means of Marangoni flows against the inclusion. This leads to a strong resistance by surfactant molecules against interfacial compression/dilation and renders the surface flow divergence free ($\boldsymbol{\nabla}_s \cdot \mathbf{u}_s = 0$) [**48**–**52**]. In general, an insoluble monolayer establishes Marangoni flows much faster than rate of surface convection (a/U) and the presence of insoluble surfactants almost always means an incompressible interface [**48**–**50**]. In a soluble monolayer, surfactants can also adsorb-desorb upon interfacial dilation-compression to balance surface concentration gradients. If the monolayer equilibrates through surfactant adsorption and desorption, then it behaves as a compressible interface [**48**, **50**]. Assuming a planar insoluble membrane, (Eq. 1.5) can be simplified to:

$$\eta \frac{\partial \mathbf{v}}{\partial z}\bigg|_{\mathrm{z=0}} = -\boldsymbol{\nabla}_s \Pi + \eta_s \boldsymbol{\nabla}_s^2 \mathbf{u}_s, \quad \boldsymbol{\nabla}_s \cdot \mathbf{u}_s = 0. \tag{1.6}$$

(Eq. 1.6) is the 2D analogue of the incompressible Stokes equations and is used for modelling long-chain phospholipids that comprise bio-membranes as they are relatively incompressible [**53**, **54**]. Finding a solution to (Eq. 1.6) is convoluted as the 2D and 3D flows couple via boundary conditions. However in systems with a shallow subphase, the lubrication approximation simplifies the 2D-3D coupling by relating the subphase velocity gradient to surface velocity and the subphase depth H [**55**]:

$$\eta \frac{\partial \mathbf{v}}{\partial z}\bigg|_{\mathrm{z=0}} = \frac{\mathbf{u}_s}{H}. \tag{1.7}$$

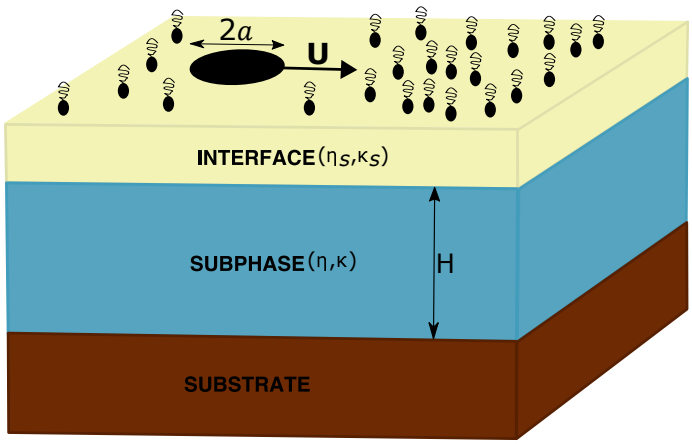

FIGURE 1.2. Schematic of a rigid disk inclusion translating on a planar surfactant-laden interface with surface shear (η_s) and dilatation (κ_s) viscosities. The interface rests on a subphase of depth H with shear and dilatation viscosities η and κ respectively. Overall, the system is supported by a rigid substrate. The translating inclusion sets up surface concentration gradients and deviates the monolayer from equilibrium. An insoluble membrane responds to this perturbation with reverse Marangoni flows around the inclusion and renders the interfacial flow field divergence free. A soluble membrane desorbs-adsorbs its surfactants to equilibrate against surface concentration gradients and exhibits incompressible behavior.

The simplification from (Eq. 1.7) is particularly useful in solving compressible-supported membrane problems where eliminating $\mathbf{u}_s$ permits analytical solutions.

1.3. Flow Regimes in 2D Hydrodynamics

Momentum propagation on interfaces shows different trends based on factors such as surface to subphase stress ratio, subphase depth and distance from the momentum source [**41**, **56**–**58**]. Scaling velocity, distance with a characteristic velocity U and probe radius a respectively, we have:

$$\frac{\eta U}{a}\frac{\partial \hat{\mathbf{v}}}{\partial \hat{z}}\bigg|_{z=0} = \frac{\eta_s U}{a^2}\left[-\hat{\boldsymbol{\nabla}}_s\hat{\Pi} + \hat{\boldsymbol{\nabla}}_s{}^2\hat{\mathbf{u}}_s\right]. \tag{1.8}$$

Here $\hat{x}$ symbolizes a non-dimensional variable x. Simplifying further gives:

$$\frac{\partial \hat{\mathbf{v}}}{\partial \hat{z}}\bigg|_{z=0} = Bq\left[-\hat{\boldsymbol{\nabla}}_s\hat{\Pi} + \hat{\boldsymbol{\nabla}}_s{}^2\hat{\mathbf{u}}_s\right], \tag{1.9}$$

where the Boussinesq number,

$$Bq = \frac{\eta_s}{\eta a}, \tag{1.10}$$

compares surface viscous stresses to subphase viscous stresses.

(Eq. 1.9) implies two distinct regimes: surface-dominant flows ($Bq \gg 1$) and subphase-dominant flows ($Bq \ll 1$). We can illustrate the fundamental differences between the two regimes by considering the paradigmatic example of a disk of radius a rotating on an interface with angular velocity $\boldsymbol{\Omega} = \Omega\hat{\boldsymbol{\theta}}$ (Fig 1.3). Such a flow does not generate surface concentration gradients and consequently, surface phenomena like Marangoni stresses, surfactant adsorption/desorption and diffusion are absent. Using the dimensional form of equation 1.9 for subphase dominant flows ($Bq \ll 1$), we get:

$$\eta \frac{\partial \mathbf{v}}{\partial z}\bigg|_{\mathrm{z=0}} = 0, \tag{1.11}$$

which is the stress-free boundary condition at the interface. Solving the 3D Stokes equation for a subphase with a stress-free interface driven by rotating disk, we get [**59**]:

$$\mathbf{u}_s(Bq \ll 1) \propto \frac{1}{r^2}\hat{\boldsymbol{\theta}} \quad \text{for } r \gg a. \tag{1.12}$$

In the case of surface dominant flows ($Bq \gg 1$) with no surface concentration gradients, (Eq. 1.9) becomes:

$$\hat{\boldsymbol{\nabla}}_s{}^2 \hat{\mathbf{u}}_s = 0. \tag{1.13}$$

Solving, we get:

$$\mathbf{u}_s(Bq \gg 1) \propto \frac{1}{r}\hat{\boldsymbol{\theta}}. \tag{1.14}$$

A viscous interface thus propagates momentum more effectively ($\propto 1/r$) in the interface-dominant regime with $Bq \gg 1$, compared to the subphase-dominant regime ($\propto 1/r^2$) with $Bq \ll 1$. This result has been verified in an experimental study from 2014 (Fig 1.3) [**60**].

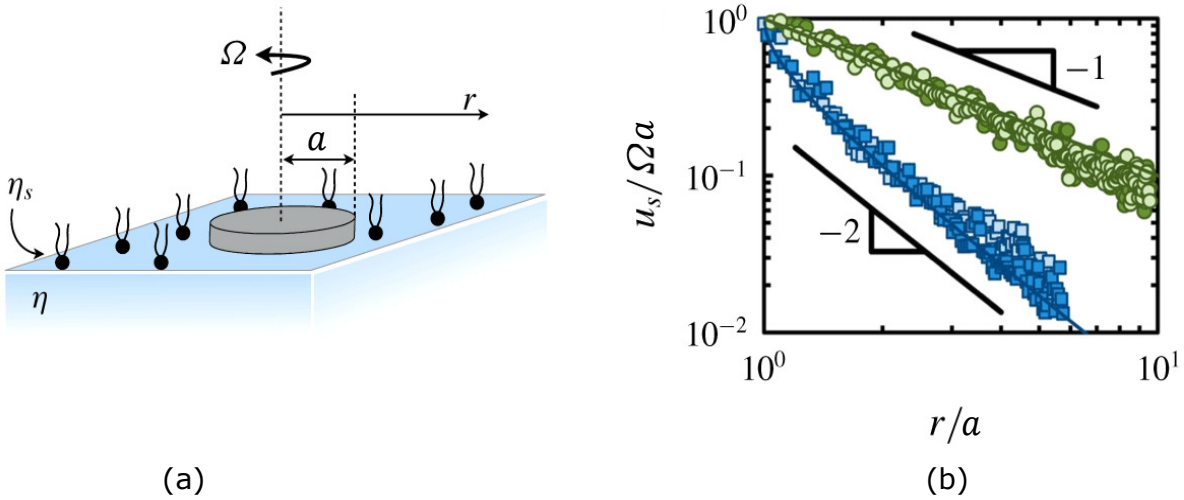

FIGURE 1.3. A disk of radius a rotating at constant angular velocity Ω on a surfactant-laden interface with surface shear viscosity η_s (b) Surface velocity u_s decays as $1/r$ when flow is interface dominant ($Bq \ll 1$, green circles) and decays as $1/r^2$ when the flow is subphase dominant ($Bq \gg 1$, blue squares); adapted from [**48**].

1.4. Momentum Crossover Length

In the interface dominant regime ($Bq \gg 1$), the incompressible 2D Stokes equation (Eq. 1.6) decouples from the 3D hydrodynamics and we have:

$$-\boldsymbol{\nabla}_s \Pi + \eta_s \boldsymbol{\nabla}_s^2 \mathbf{u}_s = 0, \quad \boldsymbol{\nabla}_s \cdot \mathbf{u}_s = 0, \tag{1.15}$$

as the corresponding governing equations.

Solving (Eq. 1.15) for an infinite cylinder translating on a 2D interface introduces the Stokes Paradox where the surface velocity scales logarithmically with distance from the disk ($|\mathbf{u}_s| \propto \log(r)$) [**61**]. Saffman, in his work from 1976 [**41**], recognized the hydrodynamic importance of the subphase and reasoned that beyond a certain distance, viscous resistance from the subphase "cuts off" the logarithmic characteristic of two-dimensional flow and the surface velocity is governed by 3D hydrodynamics ($|\mathbf{u}_s| \propto 1/r$). This regularizes the logarithmic divergence associated with the Stokes Paradox and the momentum crossover distance is known as the Saffman-Delbrück length.

$$\ell_{SD} = \frac{\eta_s}{\eta}. \tag{1.16}$$

Various experimental works [**62**–**65**] throughout the years have since corroborated the Saffman-Delbrück theory and established the cross-over between 2D and 3D hydrodynamics beyond ℓ_{SD}. For a disk translating on a free-standing membrane within the cross-over length, surface velocity is 2D-like and propagates as $\log(r)$ until the cross-over length, beyond which it follows a $1/r$ decay, like a 3D problem.

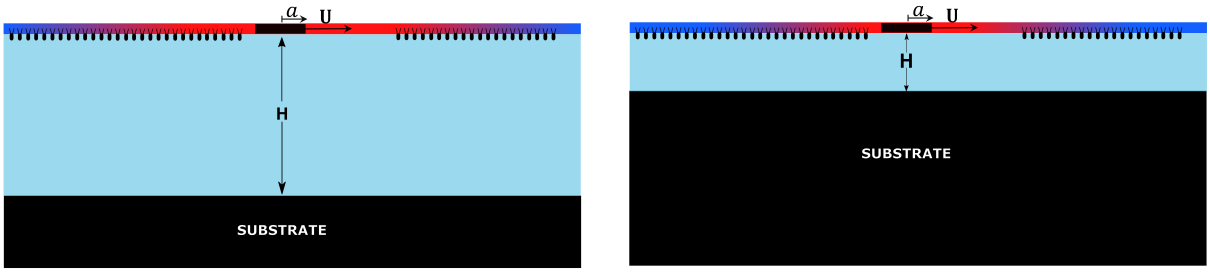

(a) (b)

FIGURE 1.4. Schematic of an inclusion of radius a translating on a surfactant-laden interface with (a) deep subphase and (b) shallow subphase. Red area on the interface represents a region within the momentum crossover length (not to scale) that is governed by 2D hydrodynamics. The blue area on the interface represents a region beyond the momentum crossover length and follows 3D hydrodynamics. The area governed by interfacial hydrodynamics is reduced for a shallow subphase.

More subtleties arise in this balance of bulk / interfacial stresses when the membrane is adjacent to a substrate so that the bulk is a thin liquid film [**55**]. The span of 2D hydrodynamics diminishes due to a no-slip velocity at the rigid substrate and the flow mimics the behavior of a mass dipole, decaying as $(1/r^2)$ [**66**, **67**]. This is similar to fluid motion in a Hele-Shaw cell. In this scenario, the subphase depth (H) plays an important role in modifying the 2D-3D momentum crossover length as [**55**, **68**] :

$$\ell_H = (\ell_{SD} H)^{1/2}. \tag{1.17}$$

There are other regimes in supported membrane problems that differ in the subphase depth versus the Saffman-Delbrück length. Velocity response functions for these regimes with $r \approx a$ and $r \gg a$ have been derived [**67**, **68**], but are beyond the scope of our discussion.

In this work, we focus our attention to free-standing membranes (subphase with infinite depth) and consider an interface (2D) dominant flow regime; i.e., we assume that inter-particle distances (r)

always stay within the Saffman-Delbrück length. However, we relax the Newtonian approximation and model the membrane to have a more realistic non-linear constitutive relation. The next section describes the non-Newtonian rheology of the membrane being modeled.

1.5. Non-Trivial Rheology of The Membrane

A surface rheological response from a membrane is difficult to interpret due to phenomena like Marangoni flow and surfactant adsorption/desorption occurring upon interfacial deformation. These surface-phenomena affect the flow-field and influence viscometric studies on a membrane. This limitation has led to extensive debate on the existence of surface rheology since the mid 19th century [**3**]. Another challenge in studying surface-rheology, stems from the intimate coupling between the interfacial and bulk flows, as discussed in §1.2-§1.4.

Multiple protocols have been developed for measuring surface shear and surface dilatational viscosity of complex fluid-fluid interfaces [**69**–**74**]. A general consideration in designing such protocols is to minimize the forces from the subphase. This can be achieved by modifying the characteristic length scale of the geometry via a decrease in size of the measurement probe [**69**, **70**]. A major contribution to this field was made in 2011 when a novel technique combining active micro-rheology and fluorescence microscopy allowed for correlation between interfacial deformation and rheology on monolayer films [**75**].

A well known departure from Newtonian fluid mechanics occurs as surface viscosity (η_s) of insoluble Langmuir monolayers change with variation in surface-pressure (Π). Viscosity changes are observed over a range of Π that is commonly accessible in experiments, unlike 3D fluids whose viscosity changes under extreme pressure only. Phospholipid dipalmitoylphosphatidylcholine (DPPC) is a major constituent of cell membranes and shows variation in η_s with Π. DPPC forms stable monolayers at an air-water interface that undergo a phase transition at a critical Π of approx. 8 mN m^{-1} at room temperature [**76**]. Above this critical surface-pressure, the monolayer viscosity is observed to increase exponentially with Π [**77**–**79**]. Similar 'Π-thickening' behavior has been observed in certain fatty acids like nonadaconic (C_{19}) acid, heneicosanoic (C_{21}) acid and behenic (C_{22}) acid [**80**]. This can be reasoned qualitatively in terms of free-area theories of viscosity [**81**].

A drop in η_s with increasing Π from 10 to 20 mN m^{-1} (Π-thinning) is observed in eicosanol membranes after attaining critical pressure of approx. 3 mN m^{-1} [**82**, **83**].

Exponential dependence of surface viscosity on surface pressure can be written as:

$$\eta_s(\Pi) = \eta_s^0 e^{\Pi - \Pi_\infty / \Pi_c}, \tag{1.18}$$

where Π_c is the characteristic surface pressure change required to produce a noticeable change in η_s, and η_s^0 is a reference viscosity at a reference pressure Π_∞, that is, $\eta_s^0 = e^{\Pi_\infty/\Pi_c}$ is the undisturbed surface viscosity of the monolayer. Then, $\Pi - \Pi_\infty$ is the 'mechanical' surface pressure that enters (Eq. 1.6) and we set $\Pi_\infty = 0$ in further development of our model in §2. We note that Π-thinning behavior can also be captured in (Eq. 1.18) by inverting the sign of the critical surface pressure (Π_c) and setting $\Pi_c \to \infty$ retrieves the Newtonian limit of constant surface viscosity.
For membranes of weakly non-Newtonian nature ($\Pi_c \uparrow$), we can linearize (Eq. 1.18) to formulate a perturbative approach in solving the governing momentum balance equations.

$$\eta_s^0 e^{\Pi/\Pi_c} = \eta_s^0 \left[1 + \frac{\Pi}{\Pi_c} + \mathcal{O}\left(\frac{\Pi}{\Pi_c}\right)^2 + ... \right] \tag{1.19}$$

This approach has been successfully used in analysing weakly non-linear effects of complex interfaces on embedded inclusions [**48**, **84**, **85**]. In the next chapter §2, we modify the governing equations for a fluid-fluid interface to account for the non-Newtonian rheology and solve the paradigmatic problem of a rigid disk translating on such an interface with a background shear flow, by using the reciprocal theorem.

CHAPTER 2

Mathematical Model

For an incompressible interface on the x-y plane, the stress balance at low Reynolds number is captured by the Boussinesq-Scriven equation [**46**]:

$$\boldsymbol{\nabla}_s\Pi = \boldsymbol{\nabla}_\mathbf{s}\cdot\left[\eta_s(\boldsymbol{\nabla}_\mathbf{s}\mathbf{u_s} + (\boldsymbol{\nabla}_\mathbf{s}\mathbf{u_s})^\mathbf{T})\right] - \eta\frac{\partial\mathbf{v}}{\partial z}\bigg|_{z=0}. \tag{2.1}$$

Here $\boldsymbol{\nabla}_s$ represents the surface gradient operator, Π is the surface pressure, η_s and η are the shear viscosity of the interface and the sub-phase respectively. The last term on the right hand side relates the sub-phase to the interface via viscous traction and is determined by solving the Navier-Stokes equation with equation (2.1) as a boundary condition.

2.1. Formulation of the non-Newtonian Model

We begin with the incompressible Boussinesq-Scriven equation for a free membrane ($Bq \gg 1$) with a pressure field Π and rate of strain $\mathbf{S}$:

$$\boldsymbol{\nabla}_s\cdot\boldsymbol{\sigma} = -\boldsymbol{\nabla}_s\Pi + \boldsymbol{\nabla}_s\cdot[\eta_s(\Pi)\mathbf{S}] = 0,\ \boldsymbol{\nabla}_\mathbf{s}\cdot\mathbf{u} = 0. \tag{2.2}$$

Here η_s is the surface viscosity and $\mathbf{u}$ is the velocity field. The exponential pressure dependence of surface viscosity on surface pressure is given by $\eta_s(\Pi) = \eta_s^0 e^{\Pi/\Pi_0}$ and has been discussed in §1.5. It is not possible to proceed by using this formulation without simplification. We take a perturbative approach in incorporating the non-linearity for small-departures of $\eta_s(\Pi)$ from η_s^0 or a high Π_c :

$$\eta_s(\Pi) = \eta_s^0 e^{\Pi/\Pi_c} = \eta_s^0\left[1 + \frac{\Pi}{\Pi_c}\right] = \eta_s^0\left[1 + \beta\frac{\Pi}{\Pi_0}\right], \tag{2.3}$$

where

$$\beta = \frac{\Pi_0}{\Pi_c}, \tag{2.4}$$

is a dimensionless parameter which is small for weak pressure dependence and vice versa. Substituting (2.2) in (2.1) we have:

$$-\boldsymbol{\nabla}_s\Pi + \boldsymbol{\nabla}_s \cdot \eta_s^0 \left[1 + \beta\frac{\Pi}{\Pi_0}\right]\mathbf{S} = 0 \Rightarrow \boldsymbol{\nabla}_s\Pi = \eta_s^0\boldsymbol{\nabla}_\mathbf{s}\cdot\mathbf{S} + \frac{\eta_s^0\beta}{\Pi_0}\boldsymbol{\nabla}_s\cdot[\Pi\mathbf{S}]. \tag{2.5}$$

Scaling distance, velocity and pressure by their characteristic scales $a, \mathbf{U}, \Pi_0 = \eta_s^0 U/a$ respectively, we have :

$$\boldsymbol{\nabla}_s\Pi = \boldsymbol{\nabla}_s\cdot\mathbf{S} + \beta\boldsymbol{\nabla}_s\cdot[\Pi\mathbf{S}]\,. \tag{2.6}$$

In the weakly non-linear limit where $\beta \ll 1$, we asymptotically expand the dimensional velocity and pressure fields as a regular expansion in β as:

$$\mathbf{u} = \mathbf{u}^{(0)} + \beta\mathbf{u}^{(1)} + \mathcal{O}(\beta^2), \tag{2.7}$$

$$\Pi = \Pi^{(0)} + \beta\Pi^{(1)} + \mathcal{O}(\beta^2). \tag{2.8}$$

Then, the expression for the corresponding non-dimensional stress tensor can be simplified as:

$$\boldsymbol{\sigma} = -\Pi\mathbf{I} + [1 + \beta\Pi]\,\mathbf{S}. \tag{2.9}$$

Using equation (2.5) and (2.6), to $\mathcal{O}(\beta)$ we have:

$$\begin{aligned}
\boldsymbol{\sigma} &= -\left(\Pi^{(0)} + \beta\Pi^{(1)}\right)\mathbf{I} + \left[1 + \beta\left(\Pi^{(0)} + \beta\Pi^{(1)}\right)\right]\left(\mathbf{S}^{(0)} + \beta\mathbf{S}^{(1)}\right), \\
\boldsymbol{\sigma} &= -\Pi^{(0)}I + \mathbf{S}^{(0)} + \beta\left(-\Pi^{(1)}\mathbf{I} + \mathbf{S}^{(1)} + \Pi^{(0)}\mathbf{S}^{(0)}\right) + \mathcal{O}(\beta^2).
\end{aligned}$$

Performing the above analysis, we obtain the following as the non-dimensional stress tensor:

$$\boldsymbol{\sigma} \quad = \boldsymbol{\sigma}^{(0)} + \beta\boldsymbol{\sigma}^{(1)} + \mathcal{O}(\beta^2), \tag{2.10}$$

$$\boldsymbol{\sigma}^{(0)} = -\Pi^{(0)}\mathbf{I} + \mathbf{S}^{(0)}, \tag{2.11}$$

$$\boldsymbol{\sigma}^{(1)} = -\Pi^{(1)}\mathbf{I} + \mathbf{S}^{(1)} + \Pi^{(0)}\mathbf{S}^{(0)}. \tag{2.12}$$

We note that the $\mathcal{O}(\beta)$ stress tensor is similar to the Newtonian stress tensor, but with an extra body force like term that depends on $\mathcal{O}(1)$ solution.

To linear order, for $\beta \ll 1$, the non-linear stress arising in the interface due to pressure dependent viscosity is given by $\boldsymbol{\sigma}^{(1)}$ and consequently, the momentum and mass conservation equations become:

$$\boldsymbol{\nabla}_s \cdot \boldsymbol{\sigma}^{(0)} = \boldsymbol{\nabla}_s \cdot \boldsymbol{\sigma}^{(1)} = 0 \tag{2.13}$$

$$\boldsymbol{\nabla}_s \cdot \mathbf{u}^{(0)} = \boldsymbol{\nabla}_s \cdot \mathbf{u}^{(1)} = 0 \tag{2.14}$$

2.2. Isolated Disk Translating in Background Shear Flow

We analyze the translation of an isolated disk of radius a at a prescribed velocity $\mathbf{U}$ in the non-Newtonian interface with an imposed linear velocity field given by:

$$\mathbf{v}(\mathbf{x}) = \mathbf{v}_0 + \mathbf{x} \cdot \mathbf{A}, \tag{2.15}$$

where $\mathbf{A} = \boldsymbol{\nabla}_s \mathbf{v} + (\boldsymbol{\nabla}_s \mathbf{v})^T$ is the rate of strain tensor of the imposed background flow. Let $q(x)$ and $\boldsymbol{\tau}(x)$ be the imposed pressure and stress field on the interface and Π and $\mathbf{S}$ be the pressure and rate of strain due to translation of the disk. When translating in the background flow field, the net velocity of the disk will be the sum of its self velocity and the mean background velocity. Assuming the origin at the centre of the disk, we have:

$$\mathbf{U}^p = \mathbf{U} + \mathbf{v}_0. \tag{2.16}$$

We aim to evaluate the non-linear correction to $\mathbf{U}^p$ in the limit of $\beta \ll 1$. This correction can be obtained by employing the Lorentz Reciprocal Theorem, which will be outlined in the next section. Let Π_t and $\mathbf{u}$ denote the total surface pressure and velocity field on the interface and $\mathcal{S}$ be the surface of the disk. Then the momentum and mass conservation equations read:

$$\boldsymbol{\nabla}_\mathbf{s} \cdot \boldsymbol{\sigma} = 0 \quad \text{and} \quad \boldsymbol{\nabla}_\mathbf{s} \cdot \mathbf{u} = 0, \tag{2.17}$$

where $\boldsymbol{\sigma}$ is the total stress field on the interface. The boundary conditions for the velocity field are:

$$\mathbf{u}(\mathbf{x}) = \mathbf{U}^p \quad \forall\, \mathbf{x} \in \mathcal{S}, \tag{2.18}$$

$$\mathbf{u}(\mathbf{x}) = \mathbf{v}(\mathbf{x}) \quad \text{as } \mathbf{x} \to \infty. \tag{2.19}$$

Following equations (2.10) - (2.12) the total stress field has the form:

$$\boldsymbol{\sigma} = \boldsymbol{\sigma}^{(0)} + \beta\boldsymbol{\sigma}^{(1)}, \tag{2.20}$$

$$\boldsymbol{\sigma}^{(0)} = -(\Pi^{(0)} + q)\mathbf{I} + (\mathbf{S}^{(0)} + \mathbf{A}), \tag{2.21}$$

$$\boldsymbol{\sigma}^{(1)} = -\Pi^{(1)}\mathbf{I} + \mathbf{S}^{(1)} + (\Pi^{(0)} + q)(\mathbf{S}^{(0)} + \mathbf{A}). \tag{2.22}$$

Similarly, the imposed stress field is modeled as:

$$\boldsymbol{\tau} = \boldsymbol{\tau}^{(0)} + \beta\boldsymbol{\tau}^{(1)}, \tag{2.23}$$

$$\boldsymbol{\tau}^{(0)} = -q\mathbf{I} + \mathbf{A}, \tag{2.24}$$

$$\boldsymbol{\tau}^{(1)} = q\mathbf{A}. \tag{2.25}$$

To evaluate the effect of the non-linear interface on disk dynamics, we seek to employ an integral formation and it is advantageous to have disturbance fields decay to zero far from the particle. So, we define the disturbance flow variables $\hat{\mathbf{u}}, \hat{\Pi}, \hat{\boldsymbol{\sigma}}$ by subtracting imposed background flow variables $\mathbf{v}(\mathbf{x})$, q, $\boldsymbol{\tau}(\mathbf{x})$ from the total flow variables $\mathbf{u}$, Π_t, $\boldsymbol{\sigma}$.

$$\hat{\mathbf{u}}(\mathbf{x}) = \mathbf{u}(\mathbf{x}) - \mathbf{v}(\mathbf{x}) \tag{2.26}$$

$$\hat{\Pi} = \Pi_t - q(\mathbf{x}) \tag{2.27}$$

$$\hat{\boldsymbol{\sigma}} = \boldsymbol{\sigma} - \boldsymbol{\tau}(\mathbf{x}) \tag{2.28}$$

These disturbance variables will also satisfy the momentum conservation and continuity equations and can be asymptotically expanded as a regular expansion in β:

$$\hat{\mathbf{u}} = \hat{\mathbf{u}}^{(0)} + \beta\hat{\mathbf{u}}^{(1)} \tag{2.29}$$

$$\hat{\Pi} = \hat{\Pi}^{(0)} + \beta\hat{\Pi}^{(1)} \tag{2.30}$$

$$\hat{\boldsymbol{\sigma}} = \hat{\boldsymbol{\sigma}}^{(0)} + \beta\hat{\boldsymbol{\sigma}}^{(1)} \tag{2.31}$$

We aim to solve the disturbance problem in the weak non-linear limit $\beta \ll 1$ and thus, solve the problems corresponding to $\mathcal{O}(1)$ and $\mathcal{O}(\beta)$ respectively.

2.3. Zeroth-order Problem

The zeroth-order $\mathcal{O}(1)$ disturbance problem corresponds to the Newtonian case of a disk translating on an interface with a linear background flow. Restricting our analysis to unidirectional shear flow, $q(x) = 0$, we can write $\hat{\mathbf{u}}^{(0)}$ as the sum of disturbance velocity due to a translating disk and disturbance velocity due to the presence of a disk in an ambient linear flow. The corresponding problem can then be written as:

$$\boldsymbol{\nabla}_s \cdot \hat{\boldsymbol{\sigma}}^{(0)} = 0, \quad \boldsymbol{\nabla}_{\mathbf{s}} \cdot \hat{\mathbf{u}}^{(0)} = 0, \tag{2.32}$$

where $\hat{\boldsymbol{\sigma}}^{(0)} = \hat{\Pi}^{(0)}\mathbf{I} + \boldsymbol{\nabla}_s\hat{\mathbf{u}}^{(0)} + \boldsymbol{\nabla}_s\hat{\mathbf{u}}^{(0)T}$ with boundary conditions:

$$\hat{\mathbf{u}}^{(0)} = \mathbf{U} \ \ \forall\, \mathbf{x} \in \ \mathcal{S}, \tag{2.33}$$

$$\hat{\mathbf{u}}^{(0)} \to 0 \ \ as \ \ |\mathbf{x}| \ \to \infty. \tag{2.34}$$

Using standard methods of 2D stokes flow, the non-dimensional velocity field can be derived as:

$$\hat{\mathbf{u}}^{(0)}(\mathbf{x}) = \mathbf{u}^{\mathrm{tr}}(\mathbf{x}) + \mathbf{u}^{\mathrm{ext}}(\mathbf{x}). \tag{2.35}$$

$$\mathbf{u}^{\mathrm{tr}}(\mathbf{x}) = \left[2\left(-\ln(r)\mathbf{I} + \frac{\mathbf{xx}}{r^2}\right) + \left(\frac{\mathbf{I}}{r^2} - \frac{2\mathbf{xx}}{r^4}\right)\right] \cdot \mathbf{U}. \tag{2.36}$$

$$\mathbf{u}^{\mathrm{ext}}(\mathbf{x}) = -\left[\frac{\mathbf{xxx}}{r^4} + \frac{1}{2}\left(\frac{\mathbf{xI}}{r^4} - \frac{2\mathbf{xxx}}{r^6}\right)\right] : \mathbf{A}. \tag{2.37}$$

Contrary to the condition in (Eq. 2.34), the velocity field from (Eq. 2.36) has a logarithmic singularity that grows as $|\mathbf{x}| \to \infty$. However, we note that beyond the momentum crossover length (§1.4), the membrane behaves like a free interface and the velocity field is governed by 3D hydrodynamics ($\hat{\mathbf{u}}^{(0)} \propto 1/r$), decaying to zero as the viscous traction from the subphase becomes dominant in the momentum balance. The effect of the non-trivial rheology of the membrane is observed within the momentum crossover length and thus justifies the use of (Eq. 2.36) in capturing membrane hydrodynamics under a high Boussinesq number ($Bq \gg 1$) regime or for distances less than the crossover length. The form of (Eq. 2.36) is an approximated form of a more complex velocity response function and is valid for distances within the crossover length ($r \ll \ell_{SD}$) [**48**].

The non-dimensional disturbance pressure field on the interface is due to disk translation and disk presence in a background flow. The solution is given by:

$$\hat{\Pi}^{(0)}(\mathbf{x}) = \Pi^{\mathrm{tr}}(\mathbf{x}) + \Pi^{\mathrm{ext}}(\mathbf{x}), \tag{2.38}$$

$$\Pi^{\mathrm{tr}}(\mathbf{x}) = \left[\frac{4\mathbf{x}}{r^2}\right] \cdot \mathbf{U}, \tag{2.39}$$

$$\Pi^{\mathrm{ext}}(\mathbf{x}) = -\left[\frac{2\mathbf{x}\mathbf{x}}{r^2}\right] : \mathbf{A}, \tag{2.40}$$

where $\mathbf{A}$ is the background rate of strain on the interface and $\mathbf{U}$ is the predefined disk velocity.

2.4. First-Order Problem

The first order problem also satisfies the momentum and continuity equations:

$$\boldsymbol{\nabla}_s \cdot \hat{\boldsymbol{\sigma}}^{(1)} = 0, \quad \boldsymbol{\nabla}_s \cdot \hat{\mathbf{u}}^{(1)} = 0. \tag{2.41}$$

with the boundary conditions:

$$\hat{\mathbf{u}}^{(1)} = \mathbf{U}^{(1)} \ \ \forall\, \mathbf{x} \in \mathcal{S}, \tag{2.42}$$

$$\hat{\mathbf{u}}^{(1)} \to 0 \ \ as \ \ |\mathbf{x}| \ \to \infty. \tag{2.43}$$

The stress tensor is given as:

$$\hat{\boldsymbol{\sigma}}^{(1)} = -\Pi^{(1)}\mathbf{I} + \mathbf{S}^{(1)} + (\Pi^{(0)} + q)(\mathbf{S}^{(0)} + \mathbf{A}) - (q\mathbf{A}). \tag{2.44}$$

Here, $\boldsymbol{\sigma}^{(1)}$ is the nonlinear stress capturing the $\mathcal{O}(\beta)$ effect of pressure dependent viscosity of the interface. In our problem setup, we choose the constraint of an imposed velocity $\mathbf{U}_p$ on the disk, which is contained in the zeroth-order solution. Therefore, the effect of pressure dependent surface rheology would yield a non-zero $\hat{\mathbf{F}}^{(1)}$, given by:

$$\hat{\mathbf{F}}^{(1)} = \int \hat{\mathbf{n}} \cdot \hat{\boldsymbol{\sigma}}^{(1)} \, dl, \tag{2.45}$$

where, $\hat{\mathbf{n}}$ is the normal vector pointing from the disk into the interface and l denotes the boundary of the domain of interest (disk).

Evaluating the non-linear effects on the disk involves solving the $\mathcal{O}(\beta)$ problem for $\hat{\mathbf{F}}^{(1)}$. We make use of the Lorentz reciprocal theorem [**86**] to get around solving the inhomogeneous equation using standard methods. The framework has previously been employed to evaluate the perturbative solution to non-Newtonian problems [**84**, **87**]. We outline the reciprocal theorem method in the following section and drop the hat notation in the further sections for convenience.

2.5. Reciprocal Theorem

In low Reynolds number dynamics, the reciprocal theorem allows for the calculation of integral quantities (force, torque) without calculating the field variables (velocity, pressure) [**86**]. We employ the reciprocal theorem to evaluate the $\mathcal{O}(\beta)$ contribution to our problem of a rigid disk translating on a weakly non-Newtonian interface with background shear. The auxiliary field $\{\Pi_{\text{aux}},\ \mathbf{u}_{\text{aux}}\ \boldsymbol{\sigma}_{\text{aux}}\}$ is considered to satisfy the homogeneous Stokes equations and represents a solution to the translation of a disc in a 2D Newtonian fluid with a velocity $\mathbf{U}_{\text{aux}}$. The solution of the auxiliary Newtonian problem is standard and is given by:

$$\mathbf{u}_{\text{aux}} = \left[2\left(-\ln(r)\mathbf{I} + \frac{\mathbf{xx}}{r^4}\right) + \left(\frac{\mathbf{I}}{r^2} - \frac{2\mathbf{xx}}{r^4}\right)\right] \cdot \mathbf{U}_{\text{aux}}, \tag{2.46}$$

$$\boldsymbol{\sigma}_{\text{aux}} = -\Pi_{\text{aux}}\,\mathbf{I} + (\nabla\mathbf{u}_{\text{aux}} + \nabla\mathbf{u}_{\text{aux}}{}^{T}), \tag{2.47}$$

$$\Pi_{\text{aux}} = \left[\frac{4\mathbf{x}}{r^2}\right] \cdot \mathbf{U}_{\text{aux}}. \tag{2.48}$$

Starting with the stokes equation for the auxiliary and $\mathcal{O}(\beta)$ problem, we have:

$$\boldsymbol{\nabla}_s \cdot \boldsymbol{\sigma}^{(1)} = 0 \quad \text{and} \quad \boldsymbol{\nabla}_s \cdot \boldsymbol{\sigma}_{\text{aux}} = 0. \tag{2.49}$$

Taking the inner product of the first equation with $\mathbf{u}_{\text{aux}}$ and the second equation with $\mathbf{u}^{(1)}$ in equation (2.49), and subtracting them, we have:

$$(\boldsymbol{\nabla}_s \cdot \boldsymbol{\sigma}^{(1)}) \cdot \mathbf{u}_{\text{aux}} - (\boldsymbol{\nabla}_s \cdot \boldsymbol{\sigma}_{\text{aux}}) \cdot \mathbf{u}^{(1)} = 0. \tag{2.50}$$

Using the chain rule of differentiation:

$$(\boldsymbol{\nabla}_s \cdot \boldsymbol{\sigma}^{(1)}) \cdot \mathbf{u}_{\text{aux}} = \boldsymbol{\nabla}_s \cdot (\boldsymbol{\sigma}^{(1)} \cdot \mathbf{u}_{\text{aux}}) - \boldsymbol{\sigma}^{(1)} : \boldsymbol{\nabla}_s \mathbf{u}_{\text{aux}}, \tag{2.51}$$

$$(\boldsymbol{\nabla}_s \cdot \boldsymbol{\sigma}_{\text{aux}}) \cdot \mathbf{u}^{(1)} = \boldsymbol{\nabla}_s \cdot (\boldsymbol{\sigma}_{\text{aux}} \cdot \mathbf{u}^{(1)}) - \boldsymbol{\sigma}_{\text{aux}} : \boldsymbol{\nabla}_s \mathbf{u}^{(1)}. \tag{2.52}$$

Substituting (2.51) and (2.52) in (2.50) we have:

$$\boldsymbol{\nabla}_s \cdot (\boldsymbol{\sigma}^{(1)} \cdot \mathbf{u}_{\text{aux}}) - \boldsymbol{\nabla}_s \cdot (\boldsymbol{\sigma}_{\text{aux}} \cdot \mathbf{u}^{(1)}) + \boldsymbol{\sigma}_{\text{aux}} : \boldsymbol{\nabla}_s \mathbf{u}^{(1)} - \boldsymbol{\sigma}^{(1)} : \boldsymbol{\nabla}_s \mathbf{u}_{\text{aux}} = 0. \tag{2.53}$$

Rearranging and integrating over the entire fluid domain S we have:

$$\int \left[\boldsymbol{\nabla}_s \cdot (\boldsymbol{\sigma}^{(1)} \cdot \mathbf{u}_{\text{aux}}) - \boldsymbol{\nabla}_s \cdot (\boldsymbol{\sigma}_{\text{aux}} \cdot \mathbf{u}^{(1)}) \right] dS = \int \left[\boldsymbol{\sigma}^{(1)} : \boldsymbol{\nabla}_s \mathbf{u}_{\text{aux}} - \boldsymbol{\sigma}_{\text{aux}} : \boldsymbol{\nabla}_s \mathbf{u}^{(1)} \right] dS. \tag{2.54}$$

Applying the 2D divergence theorem:

$$\int_S (\boldsymbol{\nabla}_s \cdot \mathbf{x}) \, dS = \int_l \hat{\mathbf{n}} \cdot \mathbf{x} \, dl. \tag{2.55}$$

The left hand side of (2.54) becomes:

$$\int \hat{\mathbf{n}} \cdot \boldsymbol{\sigma}^{(1)} \cdot \mathbf{u}_{\text{aux}} \, dl - \int \hat{\mathbf{n}} \cdot \boldsymbol{\sigma}_{\text{aux}} \cdot \mathbf{u}^{(1)} \, dl. \tag{2.56}$$

Using the boundary velocities specified in (2.42), (2.43), we simplify (2.56) as:

$$\int \hat{\mathbf{n}} \cdot \boldsymbol{\sigma}^{(1)} \cdot \mathbf{u}_{\text{aux}} \, dl - \int \hat{\mathbf{n}} \cdot \boldsymbol{\sigma}_{\text{aux}} \cdot \mathbf{u}^{(1)} \, dl = -(\mathbf{F}^{(1)} \cdot \mathbf{U}_{\text{aux}}) + (\mathbf{F}_{\text{aux}} \cdot \mathbf{U}^{(1)}). \tag{2.57}$$

From the problem setup, $\mathbf{U}^{(1)} = 0$. We extract the external non-linear force $\mathbf{F}^{(1)}$ on the disk arising due to the pressure dependent rheology of the interface. The RHS of (2.54) can be divided into two terms:

$$I_1 = \int \left[\boldsymbol{\sigma}^{(1)} : \boldsymbol{\nabla}_s \mathbf{u}_{\text{aux}} \right] dS, \tag{2.58}$$

$$I_2 = -\int \left[\boldsymbol{\sigma}_{\text{aux}} : \boldsymbol{\nabla}_s \mathbf{u}^{(1)} \right] dS. \tag{2.59}$$

Simplifying I_1 using the definition of $\boldsymbol{\sigma}^{(1)}$ (2.44) :

$$I_1 = \int \Big[(-\Pi^{(1)}\mathbf{I} + \mathbf{S}^{(1)} + (\Pi^{(0)} + q)(\mathbf{S}^{(0)} + \mathbf{A}) - q\mathbf{A}) : \boldsymbol{\nabla}_s \mathbf{u}_{\text{aux}}\Big]\, dS.$$

As a first approximation, restricting the imposed flow to unidirectional shear such that $q(\mathbf{x}) = 0$:

$$I_1 = \int \Big[-\Pi^{(1)}\nabla \cdot \mathbf{u}_{\text{aux}} + \mathbf{S}^{(1)} : \nabla \mathbf{u}_{\text{aux}} + \Pi^{(0)}(\mathbf{S}^{(0)} + \mathbf{A}) : \boldsymbol{\nabla}_s \mathbf{u}_{\text{aux}}\Big]\, dS.$$

Simplifying I_2 using $\boldsymbol{\sigma}_{\text{aux}}$ (2.49):

$$I_2 = \int \Big[(-\Pi_{\text{aux}}\, \mathbf{I} + \mathbf{S}_{\text{aux}}) :\boldsymbol{\nabla}_s \mathbf{u}^{(1)}\Big]\, dS.$$

Using continuity equations:

$$\Pi^{(1)}\mathbf{I} : \boldsymbol{\nabla}_s \mathbf{u}_{\text{aux}} = \Pi^{(1)}\boldsymbol{\nabla}_s \cdot \mathbf{u}_{\text{aux}} = 0.$$

$$\Pi_{\text{aux}}\mathbf{I} : \boldsymbol{\nabla}_s \mathbf{u}^{(1)} = \Pi_{\text{aux}}\boldsymbol{\nabla}_s \cdot \mathbf{u}^{(1)} = 0.$$

Using the identity $\mathbf{A} : \mathbf{B} = \mathbf{B} : \mathbf{A} = \mathbf{A}^{\mathbf{T}} : \mathbf{B}^{\mathbf{T}}$ we simplify:

$$\mathbf{S}^{(1)} :\boldsymbol{\nabla}_s \mathbf{u}_{\text{aux}} - \mathbf{S}_{\text{aux}} :\boldsymbol{\nabla}_s \mathbf{u}^{(1)} = 0.$$

Then (2.54) simplifies to:

$$-\mathbf{F}^{(1)} \cdot \mathbf{U}_{\text{aux}} = \int \Big[(\Pi^{(0)})(\mathbf{S}^{(0)} + \mathbf{A}) : \boldsymbol{\nabla}_s \mathbf{u}_{\text{aux}}\Big]\, dS. \tag{2.60}$$

The RHS of (Eq. 2.60) uses only the zeroth order (Newtonian) solution to solve a first order (non-Newtonian) problem. This is the magic of the reciprocal theorem in analyzing weakly non-Newtonian behaviors. We develop an analytical expression for the non-linear force by solving (Eq. 2.60) in the next section.

2.6. Non-Linear Force

We begin with the expressions for the terms in (Eq.2.60):

$$\Pi^{(0)}(\mathbf{x}) = \Pi^{\mathrm{tr}}(\mathbf{x}) + \Pi^{\mathrm{ext}}(\mathbf{x}). \tag{2.61}$$

$$\Pi^{\mathrm{tr}}(\mathbf{x}) = \left[\frac{4\mathbf{x}}{r^2}\right] \cdot \mathbf{U}. \tag{2.62}$$

$$\Pi^{\mathrm{ext}}(\mathbf{x}) = -\left[\frac{2\mathbf{xx}}{r^2}\right] : \mathbf{A}. \tag{2.63}$$

From (Eq. 2.35 - Eq. 2.37),

$$\mathbf{S}^{(0)} = (\boldsymbol{\nabla}_s \mathbf{u}^{\mathrm{tr}} + \boldsymbol{\nabla}_s \mathbf{u}^{\mathrm{tr}\,T}) + (\boldsymbol{\nabla}_s \mathbf{u}^{ext} + \boldsymbol{\nabla}_s \mathbf{u}^{\mathrm{ext}\,T}) = \mathbf{S}^{\mathrm{tr}} + \mathbf{S}^{\mathrm{ext}}, \tag{2.64}$$

where,

$$\mathbf{u}_{\mathrm{aux}} = \mathbf{u}^{\mathrm{tr}}(\mathbf{x}) = \left[2\left(-\ln(r)\mathbf{I} + \frac{\mathbf{xx}}{r^2}\right) + \left(\frac{\mathbf{I}}{r^2} - \frac{2\mathbf{xx}}{r^4}\right)\right] \cdot \mathbf{U}, \tag{2.65}$$

$$\mathbf{u}^{\mathrm{ext}}(\mathbf{x}) = -\left[\frac{\mathbf{xxx}}{r^4} + \frac{1}{2}\left(\frac{\mathbf{xI}}{r^4} - \frac{2\mathbf{xxx}}{r^6}\right)\right] : \mathbf{A}. \tag{2.66}$$

From (Eq. 2.65) we have:

$$\begin{aligned}\nabla_{\mathrm{k}} u_{\mathrm{aux(i)}} = \Bigg[&\frac{2}{r^2}(x_{\mathrm{i}}\delta_{\mathrm{jk}} + x_{\mathrm{j}}\delta_{\mathrm{ki}} - x_{\mathrm{k}}\delta_{\mathrm{ij}}) - \frac{2}{r^4}(x_{\mathrm{i}}\delta_{\mathrm{jk}} + x_{\mathrm{j}}\delta_{\mathrm{ki}} + x_{\mathrm{k}}\delta_{\mathrm{ij}}) \\ &+ \left(-\frac{1}{r^4} + \frac{2}{r^6}\right)(4x_{\mathrm{i}}x_{\mathrm{j}}x_{\mathrm{k}})\Bigg] U_{\mathrm{(aux\ j)}}.\end{aligned} \tag{2.67}$$

And from (Eq. 2.66) we get:

$$\begin{aligned}\nabla_{\mathrm{k}} u^{\mathrm{ext}}{}_{\mathrm{(i)}} = \Bigg[&\left(\frac{4}{r^6} - \frac{6}{r^8}\right) x_{\mathrm{i}}x_{\mathrm{j}}x_{\mathrm{l}}x_{\mathrm{k}} + \left(\frac{1}{r^6} - \frac{1}{r^4}\right)(x_{\mathrm{j}}x_{\mathrm{l}}\delta_{\mathrm{ik}} + x_{\mathrm{i}}x_{\mathrm{l}}\delta_{\mathrm{jk}} + x_{\mathrm{i}}x_{\mathrm{j}}\delta_{\mathrm{lk}}) \\ &+ \frac{\delta_{\mathrm{jl}}}{2}\left(\frac{x_{\mathrm{i}}x_{\mathrm{k}}}{r^6} - \frac{\delta_{\mathrm{ik}}}{r^4}\right)\Bigg] A_{\mathrm{lj}}.\end{aligned} \tag{2.68}$$

Next, we break down the terms in (Eq. 2.60) as:

$$-\mathbf{F}^{(1)} \cdot \mathbf{U}_{\mathrm{aux}} = \int \left[(\Pi^{\mathrm{tr}} + \Pi^{\mathrm{ext}})(\mathbf{S}^{\mathrm{tr}} + \mathbf{S}^{\mathrm{ext}} + \mathbf{A}) : \boldsymbol{\nabla}_s \mathbf{u}_{\mathrm{aux}}\right] dS. \tag{2.69}$$

It is convenient to convert to polar coordinates. Thus, (Eq. 2.69) becomes:

$$-\mathbf{F}^{(1)} \cdot \mathbf{U}_{\text{aux}} = \int_0^{2\pi} \int_1^{\infty} \left[(\Pi^{\text{tr}} + \Pi^{\text{ext}})(\mathbf{S}^{\text{tr}} + \mathbf{S}^{\text{ext}} + \mathbf{A}) : \boldsymbol{\nabla}_s \mathbf{u}_{\text{aux}} \right] r dr d\theta. \tag{2.70}$$

Further we note that tensors with an odd order integrate out to zero over an isotropic domain, i.e.:

$$\int_0^{2\pi} \int_1^{\infty} \mathbf{x}\ r\ dr\ d\theta = \int_0^{2\pi} n_i d\theta \int_1^{\infty} r^2 dr,$$

where $\mathbf{n_i}$ is a unit vector given by $\left[\begin{smallmatrix} \cos\theta \\ \sin\theta \end{smallmatrix} \right]$. The theta integral then gives us:

$$\begin{bmatrix} \int_0^{2\pi} \cos\theta d\theta \\ \int_0^{2\pi} \sin\theta d\theta \end{bmatrix} = 0 \Rightarrow \int_0^{2\pi} \int_1^{\infty} \mathbf{x}\ r\ dr\ d\theta = 0.$$

The above analysis can be extended to all odd ranked tensors formed from the dyadic product of unit vector n_i. Resolving the integral into a matrix, we obtain odd powers of $\sin\theta$ and $\cos\theta$ in each term, which thus integrates to zero.

$$\int_0^{2\pi} \int_1^{\infty} \mathbf{x_1 x_2 x_3 ... x_{2n-1}} = 0 \quad n \in N$$

Similarly, for even ordered tensors we have:

$$\int_0^{2\pi} \int_1^{\infty} \mathbf{xx}\ r\ dr\ d\theta = \int_0^{2\pi} n_i n_j d\theta \int_1^{\infty} r^3 dr,$$

where $n_i n_j$ are unit vectors. The theta integrals give us:

$$\begin{bmatrix} \int_0^{2\pi} \cos^2\theta d\theta & \int_0^{2\pi} \sin\theta\cos\theta d\theta \\ \int_0^{2\pi} \sin\theta\cos\theta d\theta & \int_0^{2\pi} \sin^2\theta d\theta \end{bmatrix} = b\delta_{\text{ij}}$$
$$\Rightarrow \int_0^{2\pi} \int_1^{\infty} \mathbf{xx}\ r\ dr\ d\theta = b\delta_{\text{ij}} \int_1^{\infty} r^3 dr,$$

where b is a constant. We can extend this analysis for higher (even) order tensors by equating the theta integral as a linear combination of identity tensors corresponding to the indices involved. For example,

$$\int_0^{2\pi} n_i n_j n_k n_l d\theta = C_{\text{ijkl}} = b_1 \delta_{\text{ij}} \delta_{\text{kl}} + b_2 \delta_{\text{ik}} \delta_{\text{jl}} + b_3 \delta_{\text{il}} \delta_{\text{jk}}.$$

Using the above analysis we simplify (Eq. 2.70) by removing terms that give an odd ordered tensor:

$$-\mathbf{F}^{(1)} \cdot \mathbf{U}_{\text{aux}} = \int \left[(\Pi^{\text{tr}} \mathbf{S}^{\text{ext}} : \boldsymbol{\nabla}_s \mathbf{u}_{\text{aux}}) + (\Pi^{\text{ext}} \mathbf{S}^{\text{tr}} : \boldsymbol{\nabla}_s \mathbf{u}_{\text{aux}}) + (\Pi^{\text{tr}} \mathbf{A} : \boldsymbol{\nabla}_{\mathbf{s}} \mathbf{u}_{\text{aux}}) \right] dS. \tag{2.71}$$

The above integral is not convergent for $r \to \infty$, therefore, we choose the upper limit as $R \approx \ell_{SD} \gg a$. Now it can be solved analytically and we obtain the following expression for the non-linear force (non-dimensional):

$$\mathbf{F}^{(1)} = 16\pi\xi \mathbf{U} \cdot \mathbf{A}, \tag{2.72}$$

where ξ is:

$$\xi = \log\left(\frac{R}{a}\right) - \frac{1}{4} - \frac{3}{R^2} + \frac{11}{4R^4} - \frac{1}{R^6} \tag{2.73}$$

We obtain the following expression for the leading order non-linear force (dimensional):

$$\beta \mathbf{F}^{(1)} = 16\pi \log\left(\frac{R}{a}\right) \frac{\eta_s^2}{\Pi_c} \mathbf{U} \cdot \mathbf{A}. \tag{2.74}$$

The net velocity ($\mathbf{U}$) of the disk to $\mathcal{O}(\beta)$ is given by:

$$\mathbf{U} = \mathbf{U}^{\mathbf{p}} + \mathbf{v_0}(\mathbf{x}) + \beta \mathbf{F}^{(1)} \cdot \mathbf{M}. \tag{2.75}$$

Where $\mathbf{M} = \mathbf{I_s}/4\pi\eta_s$ is the 2D mobility of the disk.

2.7. Direction and Physical Interpretation of Non-Linear Force

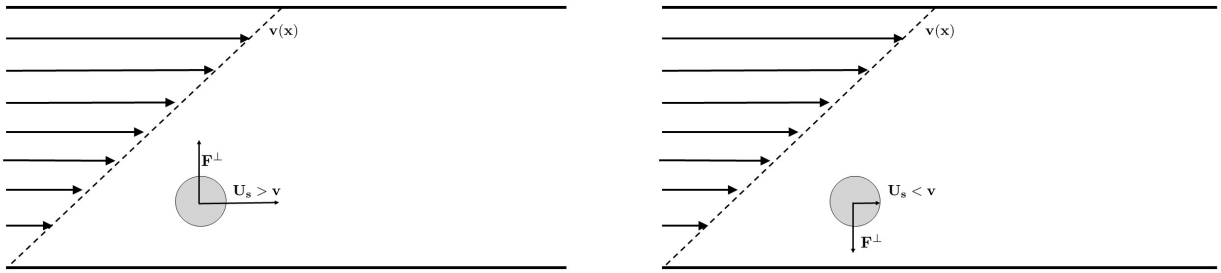

FIGURE 2.1. Direction of the non-linear force on a rigid disk when its self velocity is greater than (left) and less than (right) the background flow on the membrane. The effect of the non-linear force is compared to a similar phenomenon in 3D hydrodynamics called the Saffman lift force. it is observed that the non-linear force acts in a direction opposite to the Saffman force.

Given a disk translating with a horizontal velocity $\mathbf{U_s} = U\mathbf{e_x}$ on an interface with a background shear flow given by:

$$\mathbf{v}(\mathbf{x}) = \dot{\gamma} y \mathbf{e_x}, \tag{2.76}$$

$$\mathbf{A} = \dot{\gamma}(\mathbf{e_x e_y} + \mathbf{e_y e_x}), \tag{2.77}$$

where $\mathbf{A}$ is the background rate of strain tensor and $\mathbf{e_i}$ represents the unit vector corresponding to a direction i. We evaluate the net velocity of the disk as:

$$\mathbf{U}_p = U\mathbf{e_x} + \beta \mathbf{F}^{(1)} \cdot \mathbf{M}. \tag{2.78}$$

In the frame of the 'flowing' interface, the velocity of the disk becomes:

$$\mathbf{U}_{\text{rel}} = U\mathbf{e_x} - \mathbf{v}(\mathbf{x}). \tag{2.79}$$

Choice of a specific reference frame does not affect the physics of a system. Thus, in the moving frame of reference, the inclusion moves with a velocity $\mathbf{U}_{\text{rel}}$ and experiences a non-linear velocity (non-dimensional) given by:

$$\mathbf{U}^{(1)} = \beta \mathbf{F}_{rel}{}^{(1)} \cdot \mathbf{M}. \tag{2.80}$$

This simplifies to give:

$$\mathbf{U}^{(1)} = 4\beta\xi\dot{\gamma} U_{\text{rel}} \mathbf{e_x} \cdot (\mathbf{e_x e_y} + \mathbf{e_y e_x}) = 4\beta\xi\dot{\gamma} U_{\text{rel}} \mathbf{e_y}. \tag{2.81}$$

Therefore, the corresponding net velocity of the disk as observed from the frame of reference of the interface is:

$$\mathbf{U_p} = U_{\text{rel}} \mathbf{e_x} + 4\beta\xi\dot{\gamma} U_{\text{rel}} \mathbf{e_y}. \tag{2.82}$$

We note that the disk migrates towards the centre of the channel when $U_{\text{rel}} > 0$ and migrates towards the edge of the channel when $U_{\text{rel}} < 0$. This is summarized in (Fig. 2.1). A similar effect in weakly inertial flows of spheres through a viscous fluid with a background shear is the Saffman

lift [**41**]. In Comparison to the Saffman lift, it is seen that the non-linear force acts in a direction opposite to that of the lift force.

CHAPTER 3

Simulation Methods

In the following section, we outline the equations used to implement multi-disk simulations on a membrane with a non-linear viscous response. We will consider N disks embedded in a membrane with an infinite sub-phase, where each disk translates with a self velocity $\mathbf{U}_s$ due to an external field. This could be due to electrical, thermal or other externally applied forces. The trajectory of a disk is primarily influenced by Brownian fluctuations and the hydrodynamic disturbance field due to the other $N-1$ disks. A surface pressure field is generated due to the translation of each disk. This influences the viscosity of the membrane and broadcasts the non-linear force, derived in the previous section, to other disks. The far-field pair wise hydrodynamic interaction between disks can be approximated as the background shear flow for the non-linear force. We are interested in verifying the collective behavior of the disks under different strengths of pressure-dependent rheology (β) of the membrane.

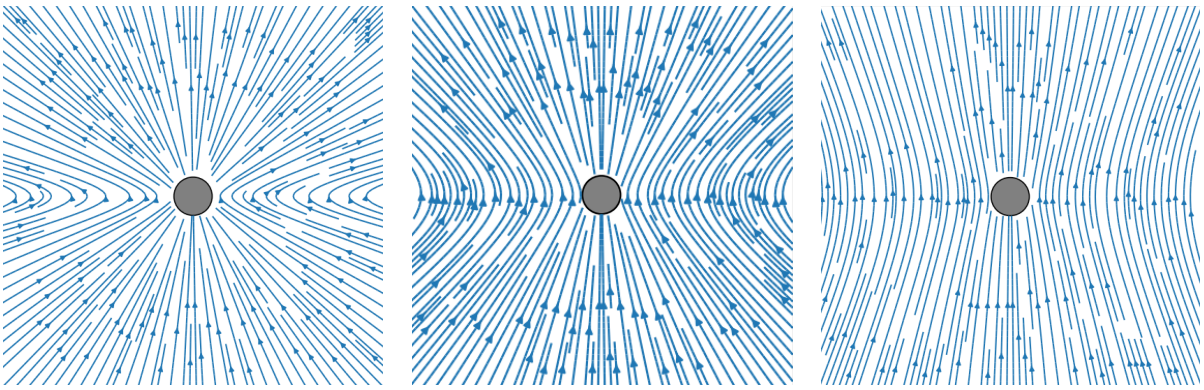

(a) (b) (c)

FIGURE 3.1. The disturbance velocity field generated by a disk translating upwards on an incompressible Newtonian membrane for $\ell_{SD}/a =$ (a) 0.1, (b) 1, (c) 10.

3.1. Brownian Dynamics

The Brownian fluctuations of each disk is influenced by its collective hydrodynamic mobility [**88**]. This is captured by the fluctuation-dissipation theorem as:

$$\langle \mathcal{U}^{\mathrm{Br}}(t)\rangle = 0, \quad \langle \mathcal{U}^{\mathrm{Br}}(t)\mathcal{U}^{\mathrm{Br}}(t')\rangle = 2k_bT\mathcal{M}\delta(t-t'). \tag{3.1}$$

Here, $\mathcal{U}^{\mathrm{Br}}$ is a vector of size $2N$ that includes the two components of $\mathbf{u}^{\mathrm{Br}}$ for all N disks. The collective mobility of the disks is included in $\mathcal{M}$, which is a $2N \times 2N$ matrix having self mobility of the disks along its diagonal and the collective mobility due to hydrodynamic interactions on its off-diagonal terms. The central 2×2 blocks along the diagonal of the collective mobility matrix ($\mathcal{M}$) are the local mobility tensor of each disk. The off-diagonal "interaction" terms only become significant at higher concentrations.

Owing to the diluteness of our system and simplicity, we only account for the local mobilities for each disk. This simplification decouples the fluctuation-dissipation relation of each disk from the rest. The translational Brownian velocities then satisfy:

$$\langle \mathbf{u_i}^{\mathrm{Br}}(t)\rangle = 0, \quad \langle \mathbf{u_i}^{\mathrm{Br}}(t)\mathbf{u_i}^{\mathrm{Br}}(t')\rangle = 2k_BT\mathbf{M}\delta(t-t'), \tag{3.2}$$

where $\mathbf{M} = \frac{1}{4\pi\eta_S^0}\mathbf{I}$ is the translational mobility of a disk. Using $\mathrm{U}^*, \mathrm{a}/\mathrm{U}^*$ as the characteristic scales for velocity and time, we obtain the Brownian velocity as:

$$\mathbf{u}_i^{\mathrm{Br}} = \mathbf{w}\sqrt{\frac{k_BT}{2\pi\eta_s^0\mathrm{U}^*a\Delta\tilde{t}}} = \mathbf{w}\sqrt{\frac{\tilde{\tau}}{2\pi\Delta\tilde{t}}}, \tag{3.3}$$

$$\tilde{\tau} = \frac{k_BT}{\mathrm{U}^*a\Delta\tilde{t}}, \tag{3.4}$$

where $\tilde{\tau}$ is a dimensionless temperature and $\mathbf{w}$ is a white noise vector containing random numbers sampled from a normal distribution of mean 0 and variance 1.

3.2. Hydrodynamic Interactions

We simulate the hydrodynamic interactions in our system such that they mimic the hydrodynamics of a free membrane (deep sub-phase) and are independent of the subphase rheology (inter-particle distance less than the 2D crossover length). The corresponding Green's function can be derived using standard methods as [**48**, **67**]:

$$G_{\mathrm{ij}}(\mathbf{r}) = \frac{1}{4\eta_s^0}\Bigg\{ \left[H_0(\tilde{r}) - \frac{H_1(\tilde{r})}{\tilde{r}} - \frac{1}{2}\left[Y_0(\tilde{r}) - Y_2(\tilde{r})\right] + \frac{2}{\pi\tilde{r}^2}\right]\delta_{\mathrm{ij}} - \left[H_0(\tilde{r}) - \frac{2H_1(\tilde{r})}{\tilde{r}} + Y_2(\tilde{r}) + \frac{4}{\pi\tilde{r}^2}\right]\frac{\mathbf{x}_{\mathrm{i}}\mathbf{x}_{\mathrm{j}}}{\tilde{r}^2}\Bigg\}, \tag{3.5}$$

where H_n are Struve functions and Y_n are Bessel functions of second kind. We note that in deriving the non-linear force we used a form of Green's function (equation (2.36)) that is derived from equation (3.5), under the condition that the inter-particle distance is well under the momentum crossover length, that is, $\tilde{r} \ll \ell_{SD}$ where ℓ_{SD} is the Saffman-Delbrück length. However, for modeling hydrodynamic interactions we use this generalized form of the velocity response function. The hydrodynamic interaction velocity on disk i due to disk j is:

$$\mathbf{u}_j(\mathbf{x}_i) = \mathbf{G}_{\mathrm{ij}}(|\mathbf{x}_i|)\cdot\mathbf{F}_{\mathrm{j}}, \tag{3.6}$$

where $\mathbf{x}_{\mathrm{i}}$ is the position vector of the i-th disk and $\mathbf{F_j}$ represents the point force on disk j.

3.3. Steric Repulsion

We add a soft repulsion between disks that get close to each other. These repulsive interactions account for the disk's excluded volume and stabilizes the singularity solution in eq. (3.5). The steric velocity is given by

$$\mathbf{u}_{\mathrm{i}}|_{\mathrm{steric}} = U_s\frac{e^{-\beta(r-L)}}{1+e^{-\beta(r-L)}}\hat{\mathbf{r}}_{\mathrm{ij}}, \tag{3.7}$$

where U_s is the contact velocity of two disks that decays exponentially over a length scale β^{-1}. From figure (3.2.) we note that hydrodynamics dominates at all inter-particle distances except near contact.

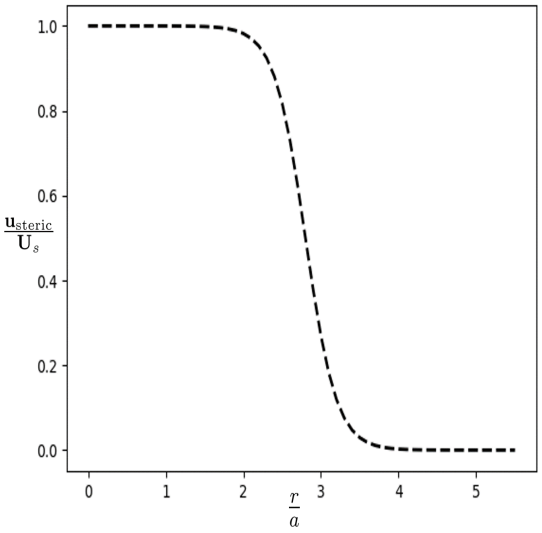

FIGURE 3.2. Steric velocity behavior with change in inter-center distance of particles. The potential is modeled such that two inclusions are not allowed to overlap. The steric effect between two disks is negligible beyond inter-particle distance of 1 radius length

3.4. Non-Linear Force

Translation of disks alters the surface pressure distribution on the membrane. This phenomenon changes surface viscosity of the membrane and consequently, an extra non-linear force acts on other disks. The net hydrodynamic disturbance due to disk i acts as a background flow for disk j. The dimensionless weakly non-linear force as developed by the reciprocal theorem approach in §2.7 is given by:

$$\mathbf{F}^{(1)} = \beta 16\pi \mathbf{U}_s \cdot (\mathbf{S}^{tr} + \mathbf{S}^{ext}), \tag{3.8}$$

where $\mathbf{S}^{tr}$and $\mathbf{S}^{ext}$ are rate of strain tensors corresponding to $\mathbf{u}^{tr}$and $\mathbf{u}^{ext}$ respectively. The non-linear velocity is obtained from the inner-product of non-linear force with the dimensionless 2D mobility of the disk, given as:

$$\mathbf{U}^{(1)} = \mathbf{F}^{(1)} \cdot \mathbf{M}, \tag{3.9}$$

$$\mathbf{M} = \frac{1}{4\pi}\mathbf{I_s}. \tag{3.10}$$

3.5. Langevin Equations

In summary, the net velocity of a disk is due to the combined effect of its self velocity, brownian fluctuations, hydrodynamic interactions, steric forces and the non-linear force. The corresponding Langevin equation reads:

$$\frac{d\mathbf{x}_i}{dt} = \mathbf{U}_s + \mathbf{u}_i^{\mathrm{Br}} + \sum_{i \neq j}^{N} \left[\mathbf{u}_j(\mathbf{x}_i) + \mathbf{u}_{ij}|_{\mathrm{steric}} + \beta \mathbf{F}_{\mathrm{ij}}{}^{(1)} \cdot \mathbf{M}_{\mathrm{i}} \right]. \tag{3.11}$$

We use (explicit) forward Euler time stepping in simulating the system. It is given by:

$$x_{(t+dt)} = x_t + \frac{dx}{dt}\,\Delta t + O((\Delta t)^2). \tag{3.12}$$

The global error associated with this time marching scheme for simulating n time-steps is of the order Δt. The choice of a small Δt makes this magnitude of error tolerable in understanding the approximate effect of the non-linear force on the collective behavior of the disks.

3.6. Packing Order Parameter

An attribute of the non-linear force on the collective dynamics of disks is the formation of clusters with crystal like order. As we shall see in chapter 4, we investigate the type of packing observed in the clusters by evaluating the n-th packing order parameter given by:

$$\Psi_n^j = \frac{1}{n_j} \sum_k e^{in\theta_{kj}}. \tag{3.13}$$

Ψ_n^j measures the orientation and the packing order around the particle j, where n_j is its nearest neighbors and θ_{kj} is the angle between the line joining disks k, j and the x-axis. The average local $\langle|\Psi_n^j|\rangle$ and global $|\langle\Psi_n^j\rangle|$ parameters quantify the packing order, with 0 representing an unordered aggregate and 1 represent a perfect n-th order aggregate. The local order parameter tells us whether each particle in an aggregate forms a n-th order lattice with its nearest neighbor. The global order parameter on the other hand, provides information on the orientation of each lattice in the aggregate.

CHAPTER 4

Results

In the present chapter, we discuss the results obtained from the simulation of multiple disks translating on a membrane with a non-linear viscous response. For a given set of parameters (β, $\tilde{\tau}$), ten different ensembles were simulated. The simulation box was programmed to move with the self velocity of the disks, thus capturing the multi-disk hydrodynamics without the need of periodicity. This setup of a "moving simulation box", enhanced the computational efficiency of the simulations and enabled us to explore the dynamics for a longer simulation time. For the following subsections, we define two disks to be connected if their inter-centre distance is less than or equal to 3.5 times the disk radius. Further, we define a disk cluster as a group of four or more connected disks.

4.1. Non-Linear Viscous Response Leads to Self Assembly of Disks

One stark difference between the Newtonian ($\beta = 0$) and the non-Newtonian ($\beta \neq 0$) simulations was that the disks self assembled to form aggregates while translating on a membrane with surface-pressure dependent rheology. Self assembly of disks was observed for all the dimensionless temperatures tested ($\tilde{\tau} \in [0.0005, 0.01]$) across ten different ensembles.

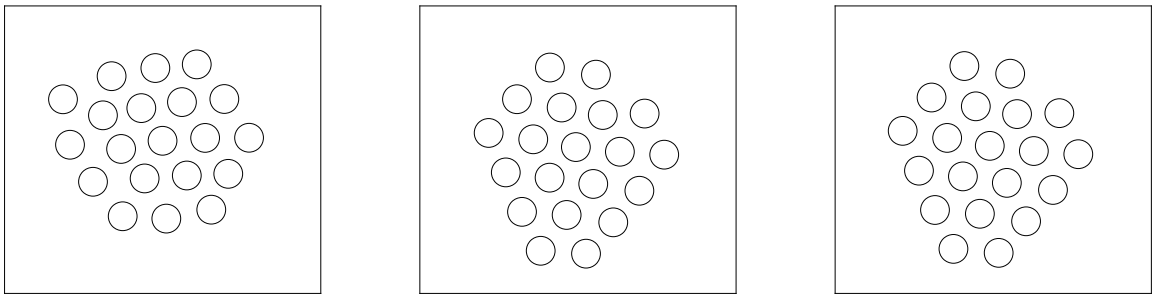

(a) $\tilde{\tau} = 0.01$ (b) $\tilde{\tau} = 0.001$ (c) $\tilde{\tau} = 0.0005$

FIGURE 4.1. Crystallized disk aggregates observed in the non-Newtonian simulation of an ensemble of disks for different dimensionless temperature $\tilde{\tau}$. The state shown is at a simulation time of $\tilde{t} = 30$ for $\beta = 0.1$. The aggregates display dynamic patterns during the simulations and crystallize with a distinct packing order §4.2.

Disk aggregates were stable and did not disintegrate for longer simulation times (as observed till $\tilde{t} = 120$). This aggregation of disks can be correlated to non-linear viscous response of the membrane, as an ensemble of disks crystallizes under non-Newtonian conditions and remains staggered under Newtonian conditions (fig 4.2).

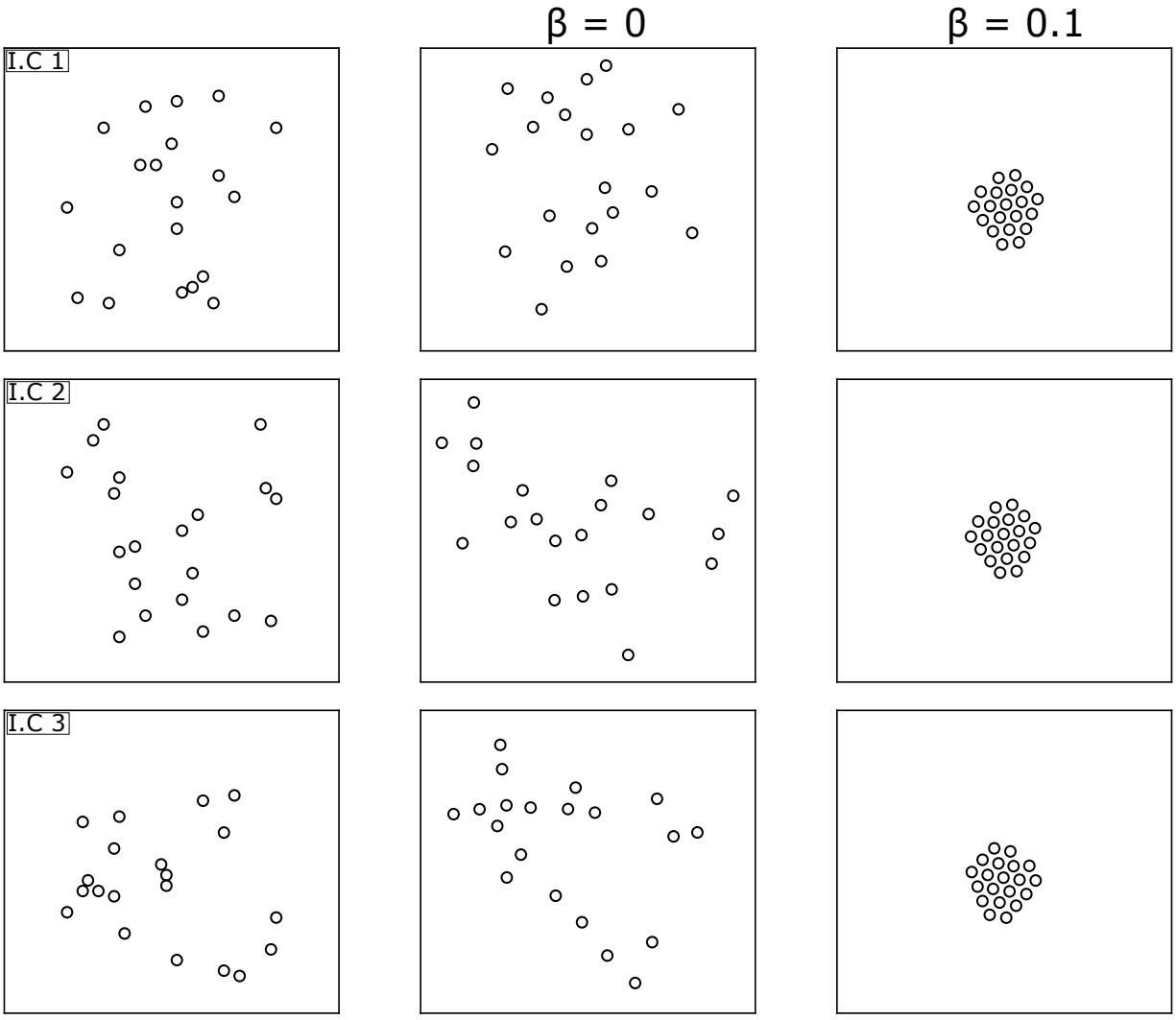

FIGURE 4.2. Snapshots of simulation box for different ensembles with $\tilde{\tau} = 0.001$. The left column shows snapshot of the initial state ($\tilde{t} = 0$) of the ensemble. The middle and right columns show snapshot of the final state ($\tilde{t} = 30$) of ensembles at $\beta = 0$ and $\beta = 0.1$ respectively. We observe crystallized aggregates in non-Newtonian simulations (right) whereas the Newtonian case (centre) yields staggered states. This observation strongly signifies the role of pressure dependent rheology of membranes in crystallization of translating rigid inclusions.

4.2. Disk crystals have hexagonal packing order

We evaluated different packing order parameters (ψ_n) of disk crystals using equation (3.13) and observed a dominant hexagonal packing order across all ensembles (see fig 4.3). Other studies [**89**, **90**] have shown rigid inclusions rotating on a membrane to form stable hexagonal crystals. It is also well known that similar systems with long ranged repulsive interaction form a stable hexagonal crystal lattice (Wigner Crystal) [**91**]. However, the only long ranged force in our study comes from hydrodynamic interactions. Citing the discussion in §4.1, we can then deduce that Newtonian hydrodynamic interactions do not lead to crystallization [**89**]. Thus, the only other long ranged interaction in our study i.e. the non-Newtonian hydrodynamic force, arising due to surface-pressure dependent rheology, leads to hexagonal disk crystals. As evident from figure 4.3, the crystals at higher temperatures ($\tilde{\tau}$) have a lower hexagonal packing order. This is expected as at a higher temperature, Brownian fluctuations are stronger and destabilize crystal order §4.4.

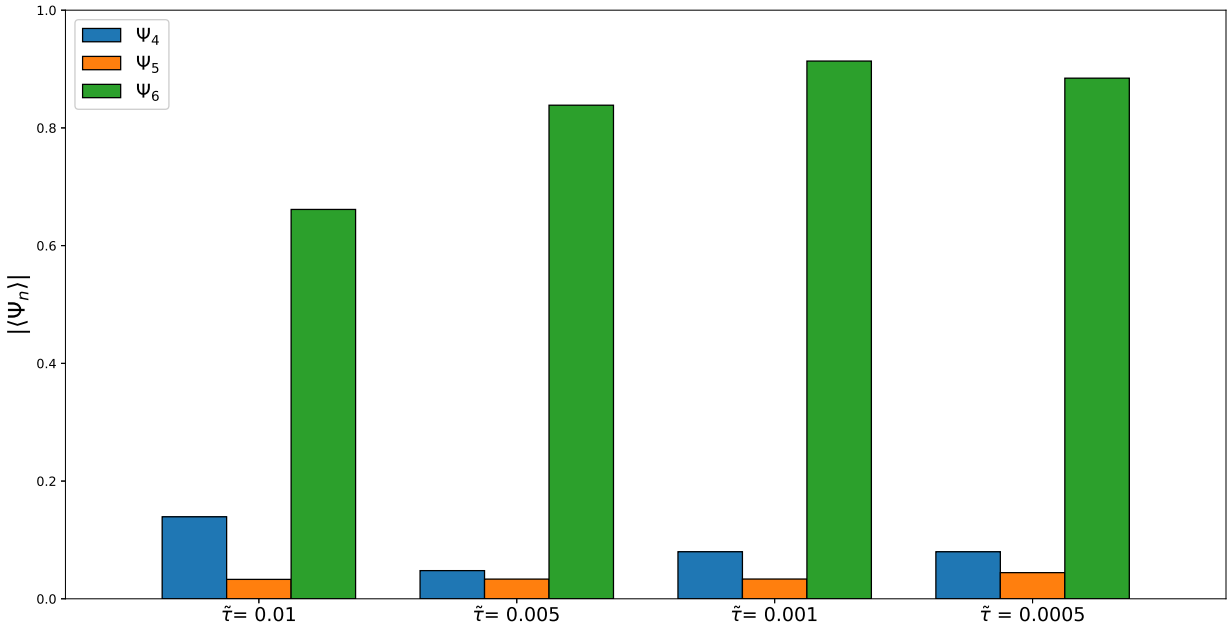

FIGURE 4.3. Comparison of different packing order in crystals formed by a particular ensemble of disks at varying temperatures ($\tilde{\tau}$) for $\beta = 0.1$. The crystals showed a dominant hexagonal packing order in comparison to square and pentagonal order. Hexagonal crystallization of disks is attributed to the non-Newtonian response of the membrane as it is not seen in the Newtonian case. Crystal order reduced at higher temperatures due to the destabilizing effect of Brownian fluctuations.

4.3. Crystals Attain a Stable Hexagonal Order With Time

Hexagonal order of the disk crystals plateaued with time and attained a stable magnitude (see fig 4.4). At any temperature, as the membrane became more non-Newtonian ($\beta \uparrow$), the crystal order stabilized faster. However, disks translating on membranes with very weak non-Newtonian nature $\beta \in (0, 0.01)$, formed stable hexagonal crystals after a significantly higher time. During isothermal translation of rigid disks on a non-Newtonian membrane, it was seen that increasing values of β yielded a crystals with higher hexagonal order. These observation corroborate the claim of non-Newtonian interactions inducing the formation of hexagonal crystals, as increasing the strength of such interactions led to an increase in the order and rate of crystallization in all ensembles.

In extending this intuition to membrane trapped proteins, rafts and motors, we expect our rigid disks to be in the 100nm range, and are thus sensitive to thermal forces. A rise in temperature increases Brownian fluctuations and since all disks on the membrane are coupled hydro-dynamically, the random fluctuations add to the inter-disk interactions. Due to its unpredictable nature, any ordered crystal lattice is destabilized with an increase in thermal noise. This can be observed in fig (4.4) as the hexagonal order of crystals show more variability irrespective of the increase in non-Newtonian nature of the membrane (β). The magnitude of hexagonal packing order in crystals also decreases at higher temperature.

Qualitatively, we observe that non-Newtonian response of the membrane induces hexagonal crystallization of disks. This is opposed by thermal noise, which brings randomness and suppresses any ordered state to be dominant across ensembles.

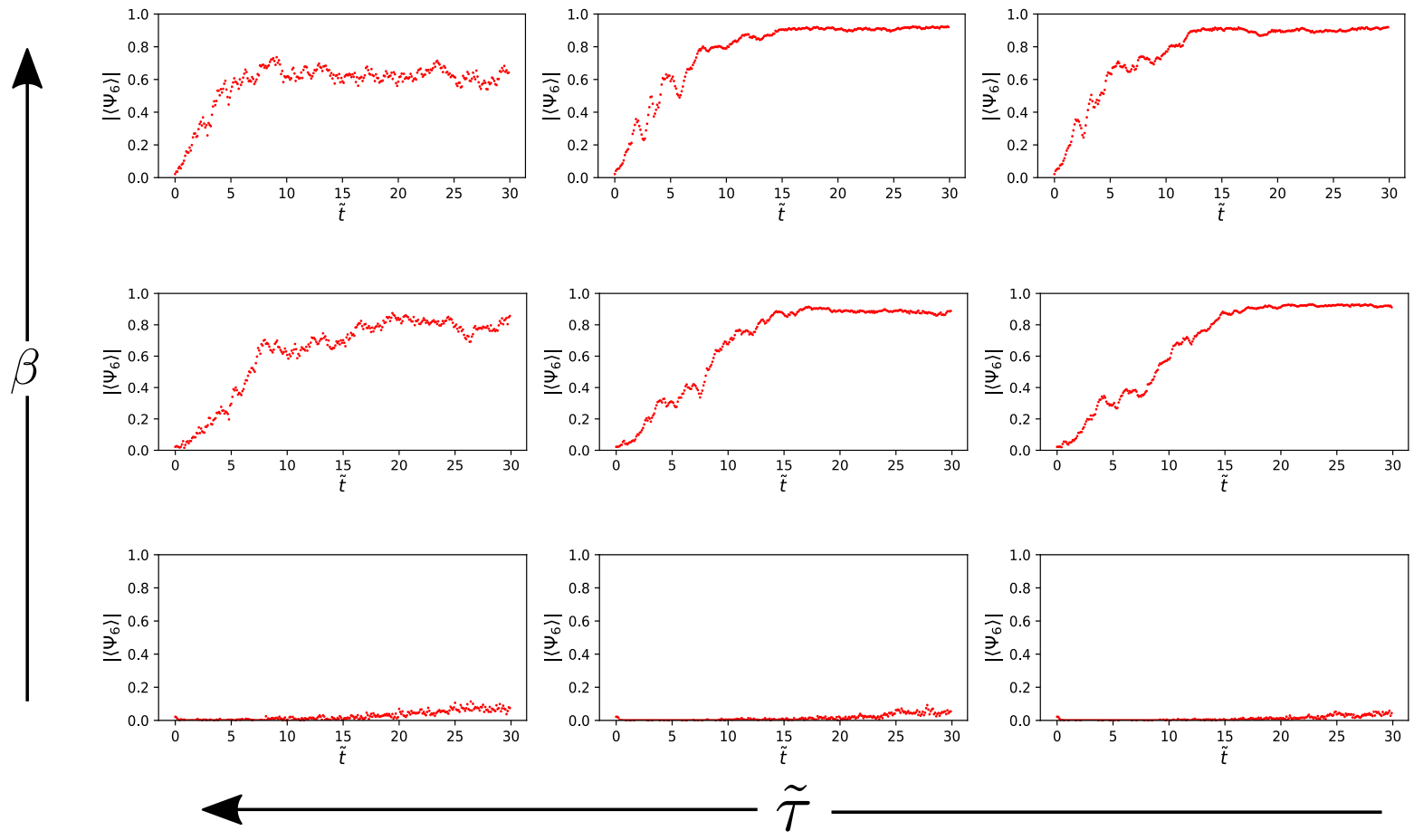

FIGURE 4.4. Plots of global hexagonal packing order parameter ($|\langle\Psi_6\rangle|$) averaged across ten ensembles, against the simulation time ($\tilde{t}$) for different system parameters ($\beta, \tilde{\tau}$). The values of β used are 0.01 (bottom row), 0.05 (mid row) and 0.1 (top row) and the values of $\tilde{\tau}$ are 0.0005 (right column), 0.001 (centre column) and 0.01 (left column). It is observed that the non-Newtonian nature of the membrane induces hexagonal crystal formation and influences the rate of crystallization. Thermal forces bring randomness to the system as Brownian kicks get stronger, leading to a reduced and fluctuating order in the crystal lattices. Overall, the hexagonal order is observed to plateau at a stable value that is influenced by thermal forces and the non-Newtonian nature of the membrane.

4.4. Influence of Rheology on Disk Crystals

Plateau value of averaged global and local hexagonal order parameters in disk crystals was observed to vary with β. A stronger surface-pressure dependent rheology of the membrane yielded highly ordered crystals under isothermal simulations. It is evident from figure (4.5a-b) that introducing non-Newtonian rheology (by increasing β) induced crystallization in rigid disk translating on a membrane. High values of the local hexagonal orientation parameter suggest that each disk formed a hexatic lattice with its nearest neighbours (figure 4.5a). Upon the formation of hexatic lattices, the disk aggregate was observed to rotate such that the lattices had a similar orientation, thus attaining an overall rotational order. This trend is captured in (figure 4.5b), where high values of global order parameters are obtained. Similar results have been obtained in other studies [**89**, **92**, **93**] where, presence of a long ranged interaction (non-Newtonian force due to surface pressure dependent rheology in our case) results in aggregation and the formation of crystals with hexatic order.

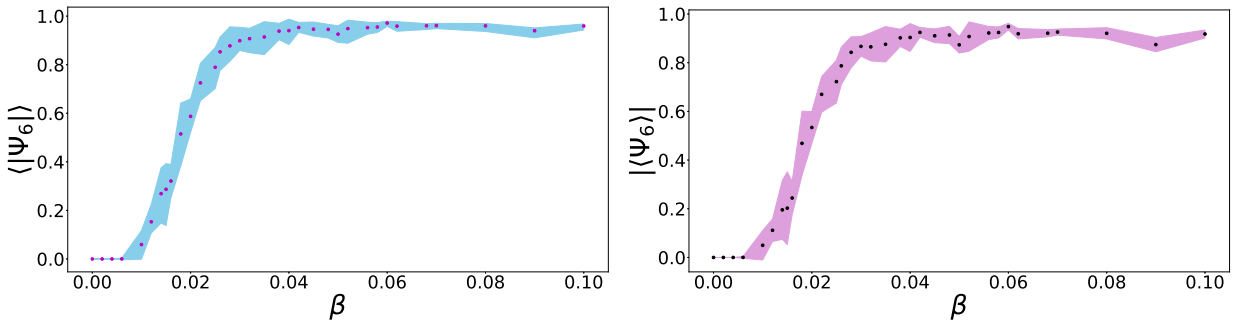

(a) (b)

FIGURE 4.5. (a) Local $\langle|\Psi_6|\rangle$ and (b) Global $|\langle\Psi_6\rangle|$ hexagonal packing order parameter of disk crystals as a function of $\beta = \Pi_0/\Pi_c$. Each data point is averaged across ten ensembles of twenty rigid disks translating isothermally on a membrane for a simulation time of $\tilde{t} = 30$. The shaded region represents the standard deviation of the respective parameters. (a) Local order being close to 1 suggests that each disk in the aggregate forms a hexatic lattice with its nearest neighbours. This parameter however, does not provide details about the orientation of lattices. (b) A high global order parameter indicates that each hexatic lattice in the disk crystal had the same orientation. Combining the local and global parameters, it is inferred that an increase in β leads to the formation of hexatic disk crystals with a high local and global order.

4.5. Thermal Forces Deter Formation of Ordered Aggregates

Rigid disks in our system are small ($\mathcal{O}$(10-100 nm)) and undergo brownian motion. Thermal fluctuations in one disk affects other disks as they interact via the fluid hydrodynamically. In general, these random interactions increase disorder and limit the self assembly of disks into ordered crystals. Another argument supporting this claim comes from the field of statistical mechanics where, an increase in temperature of a system of particles, increases its number of accessible microstates. This leads to an increase in entropy and thus, reduced order in the system. From (Fig 4.6), trends consistent with our expectations are obtained where, disk lattices at higher temperatures show lower hexatic order. The aggregates also experience a loss in global orientatinal order.

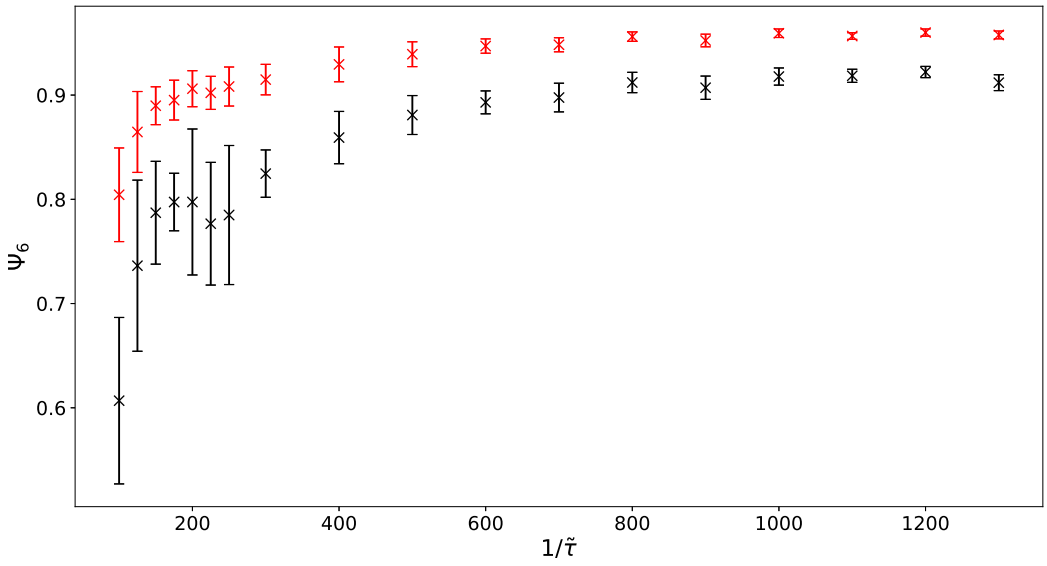

FIGURE 4.6. Effect of thermal forces on global (black) and local (red) order parameters in a system of 20 rigid disks translating on a membrane with $\beta = 0.1$. The error bars are scaled to standard deviation of respective parameters across ten ensembles for each value of $\tilde{\tau}$. The trend in local order parameter indicates that an increase in temperature impedes the formation of hexatic lattices. This is accompanied by a reduced global orientation order in the rigid disk crystal. At higher temperatures, thermal forces introduce stronger brownian fluctuations and thus, larger deviation in the ensemble averaged order parameter is observed.

CHAPTER 5

Conclusions

Surfactants play a major role in day to day biological functions. For example, pulmonary surfactants lining the alveoli maintain a critical surface tension of 2 mN/m at the end of expiration and prevent post-exhalation alveolar collapse [**94**]. Adapting our model to account for the rheological properties of alveolar lining liquid, its geometry and adsorption/desorption dynamics, we could potentially use it in designing synthetic surfactant replacement therapies to treat respiratory disorders in infants and adults [**95**]. Another interesting instance of our model's applicability is in the collective dynamics of trans-membrane proteins like ATP-synthase. Experimental studies have shown lattice formation by ATP-synthases in lipid vesicles and mitochondria [**96**–**98**]. Again, accounting for curvature and dimerization, our model can simulate such systems and provide insights into the behavior of ATP-synthase under various physical conditions. The concepts underlined in our model have been used in developing bio-interface rheological devices to study permeability of biological lipid membranes by applying shear stress from spinning disks on the lipid membrane [**99**].

A system of rigid disks translating uniformly at low Reynolds number on a free-standing, planar, non-Newtonian membrane with surface-pressure dependent viscosity, self assembles into aggregates with hexagonal order because of non-Newtonian hydrodynamic interactions arising due to membrane rheology. The hexatic order of aggregates increases with time and stabilized upon the formation of a disk crystal. A higher hexatic order is obtained in disk crystals formed on membranes whose shear viscosity (η_s) has a stronger surface-pressure dependence. The system of disks is also observed to exhibit faster crystallization with an increase in the non-Newtonian force ($\beta \uparrow; \mathbf{U_s} \uparrow$). Thermal forces destabilize the hexagonal order of disk aggregates as higher thermal activity increases the Brownian fluctuations of individual disks and enables them to sample additional microstates, thus increasing disorder.

Further work is required to improve the depth and breadth of our simulation model to mimic real-life scenarios efficiently. For example:

- Incorporating the velocity response function for a pinned membrane in derivation of the non-Newtonian force would enable us to explore dynamics of systems with low to moderate Boussinesq numbers and also help in analysing collective dynamics beyond the Saffman-delbrück length.
- Including an isotherm to capture compression/dilation induced surfactant desorption/adsorption would increase the applicability of our model in analysing compressible interfaces with surface-pressure dependent viscosity.
- Simultaneous rotation and translation of a disk embedded in a non-Newtonian monolayer, leads to a net force on the disk in a direction perpendicular to its translation [**84**]. Including this effect would also add breadth to our model in analysing active viscous inclusions.
- Rigid disks are relatively straight forward to model, but membrane inclusions can have a more complex shapes (ellipsoids) or may deform. Exploring the effect of aspect ratio and flexibility on the collective behavior would also benefit in mimicking real life systems.
- Additional analyses on collective dynamics of disks can be performed to unravel key trends. Investigating special cases like inclusions of disperse size translating on a monolayer, dynamics on an interface atop a subphase of variable depth, non-planar interfaces etc will expand our understanding of non-Newtonian 2D hydrodynamics.
- Computational efficiency is key in simulation based studies as it dictates the size and robustness of the system being simulated. Although our code used vectorized operations and low time complexity algorithms, larger systems with N^2 time cost might be prohibitive. By employing GPU accelerated parallel computing, bigger systems with multiple physics phenomena (Charged disks, Thermal gradient on membrane etc.) can be simulated efficiently.

Bibliography

[1] D. Fennell Evans and Håkan Wennerström. *The Colloidal Domain: Where Physics, Chemistry, Biology, and Technology Meet.* Wiley, February 1999.

[2] Young Thomas. An essay on the cohesion of fluids. *Phil. Trans. R. Soc.*, page 9565–87, January 1805.

[3] Scriven L.E. and Sterling C.V. The marangoni effects. *Nature*, 187:186–188, 1960.

[4] Leal LG. *Advanced transport phenomena.* Cambridge University Press., 2007.

[5] D. Langevin. Rheology of adsorbed surfactant monolayers at fluid surfaces. *Annual Review of Fluid Mechanics*, 46(1):47–65, 2014.

[6] Fuller GG and Vermant J. Complex fluid-fluid interfaces: rheology and structure. *Annu Rev Chem Biomol Eng.*, 3:519–43, 2012.

[7] P.J Wilde. Interfaces: their role in foam and emulsion behaviour. *Current Opinion in Colloid & Interface Science*, 5(3):176–181, 2000.

[8] Georgieva D, Schmitt V, Leal-Calderon F, and Langevin D. On the possible role of surface elasticity in emulsion stability. *Langmuir*, 19;25(10):5565–73, May 2009.

[9] Maldonado-Valderrama, Julia, Alberto Martín-Molina, Antonio Martín-Rodriguez, Miguel A. Cabrerizo-Vílchez, María J. Gálvez-Ruiz, and Dominique Langevin. Surface properties and foam stability of protein/surfactant mixtures:theory and experiment. *The Journal of Physical Chemistry C*, 111(6):2715–2723, 2007.

[10] Anne-Laure Fameau and Anniina Salonen. Effect of particles and aggregated structures on the foam stability and aging. *Comptes Rendus Physique*, 15(8):748–760, 2014. Liquid and solid foams / Mousses liquides et solides.

[11] R. Phillips. *Physical Biology of the Cell.* Garland Science, 2013.

[12] Rahul Grover, Janine Fischer, Friedrich W Schwarz, Wilhelm J Walter, Petra Schwille, and Stefan Diez. Transport efficiency of membrane-anchored kinesin-1 motors depends on motor density and diffusivity. *Proceedings of the National Academy of Sciences of the United States of America*, 113(46):E7185—E7193, November 2016.

[13] Campàs O, Leduc C, Bassereau P, Casademunt J, Joanny JF, and Prost J. Coordination of kinesin motors pulling on fluid membranes. *Biophys J.*, 94(12):5009–5017, 2008.

[14] Alexander S. Mikhailov and Raymond Kapral. Hydrodynamic collective effects of active protein machines in solution and lipid bilayers. *Proceedings of the National Academy of Sciences*, 112(28):E3639–E3644, 2015.

[15] Eric Dickinson. Hydrocolloids at interfaces and the influence on the properties of dispersed systems. *Food Hydrocolloids*, 17(1):25–39, 2003.

[16] W. Ramsden and Francis Gotch. Separation of solids in the surface-layers of solutions and suspensions (observations on surface-membranes, bubbles, emulsions, and mechanical coagulation). *Proceedings of the Royal Society of London*, 72(477-486):156–164, 1904.

[17] Spencer Umfreville Pickering. Cxcvi.—emulsions. *J. Chem. Soc., Trans.*, 91:2001–2021, 1907.

[18] van Meer G, Voelker DR, and Feigenson GW. Membrane lipids: where they are and how they behave. *Nat Rev Mol Cell Biol.*, 9(2):112–24, February 2008.

[19] Zasadzinski JA, Ding J, Warriner HE, Bringezu F, and Waring F. The physics and physiology of lung surfactants. *Curr. Opin. Colloid Interface Sci.*, 6:506–13, 2001.

[20] Kühlbrandt W. Structure and function of mitochondrial membrane protein complexes. *BMC Biol*, 13(89), October 2015.

[21] Y Shi, E Sezgin, and W Chen. Editorial: The role of biomembranes and biophysics in immune cell signaling. *Front. Immunol.*, 12:740373, September 2021.

[22] Orbach R and Su X. Surfing on membrane waves: Microvilli, curved membranes, and immune signaling. *Front. Immunol.*, 11:2187, August 2020.

[23] Steven L. Percival, Dieter Mayer, Robert S. Kirsner, Greg Schultz, Dot Weir, Sashwati Roy, Afsaneh Alavi, and Marco Romanelli. Surfactants: Role in biofilm management and cellular behaviour. *International Wound Journal*, 16(3):753–760, 2019.

[24] Daniels R, Reynaert S, Hoekstra H, Verreth C, Janssens J, Braeken K, Fauvart M, Beullens S, Heusdens C, Lambrichts I, De Vos DE, Vanderleyden J, Vermant J, and Michiels J. Quorum signal molecules as biosurfactants affecting swarming in rhizobium etli. *Proc. Natl. Acad. Sci. U S A.*, 103(40):14965–70, October 2006.

[25] M. Fauvart, P. Phillips, D. Bachaspatimayum, N. Verstraeten, J. Fransaer, J. Michiels, and J. Vermant. Surface tension gradient control of bacterial swarming in colonies of pseudomonas aeruginosa. *Soft Matter*, 8:70–76, 2012.

[26] Angelini TE, Roper M, Kolter R, Weitz DA, and Brenner MP. Bacillus subtilis spreads by surfing on waves of surfactant. *Proc Natl Acad Sci U S A*, 106(43):18109–13, October 2009.

[27] Singer SJ and Nicolson GL. The fluid mosaic model of the structure of cell membranes. *Science*, 18;175(4023):720–31, February 1972.

[28] Edward J. Shimshick and Harden M. McConnell. Lateral phase separation in phospholipid membranes. *Biochemistry*, 12(12):2351–2360, 1973.

[29] O. G. Mouritsen and M. Bloom. Mattress model of lipid-protein interactions in membranes. *Biophys J*, 46(2):141–153, August 1984.

[30] E. Oldfield and D. Chapman. Dynamics of lipids in membranes: Heterogeneity and the role of cholesterol. *FEBS Letters*, 23(3):285–297, 1972.

[31] K. Simons and E. Ikonen. Functional rafts in cell membranes. *Nature*, 387(6633):569–572, Jun 1997.

[32] Susana A. Sanchez, Maria A. Tricerri, and Enrico Gratton. Laurdan generalized polarization fluctuations measures membrane packing micro-heterogeneity in vivo. *PNAS*, 109(19):7314–7319, 2012.

[33] Riya Raghupathy, Anupama Ambika Anilkumar, Anirban Polley, Parvinder Pal Singh, Mahipal Yadav, Charles Johnson, Sharad Suryawanshi, Varma Saikam, Sanghapal D. Sawant, Aniruddha Panda, Zhongwu Guo, Ram A. Vishwakarma, Madan Rao, and Satyajit Mayor. Transbilayer lipid interactions mediate nanoclustering of lipid-anchored proteins. *Cell*, 161(3):581–594, 2015.

[34] Prabuddha Sengupta, David Holowka, and Barbara Baird. Fluorescence resonance energy transfer between lipid probes detects nanoscopic heterogeneity in the plasma membrane of live cells. *Biophysical Journal*, 92(10):3564–3574, 2007.

[35] Masanao Kinoshita, Kenichi G.N. Suzuki, Nobuaki Matsumori, Misa Takada, Hikaru Ano, Kenichi Morigaki, Mitsuhiro Abe, Asami Makino, Toshihide Kobayashi, Koichiro M. Hirosawa, Takahiro K. Fujiwara, Akihiro Kusumi, and Michio Murata. Raft-based sphingomyelin interactions revealed by new fluorescent sphingomyelin analogs. *Journal of Cell Biology*, 216(4):1183–1204, 03 2017.

[36] Jessica F. Frisz, Kaiyan Lou, Haley A. Klitzing, William P. Hanafin, Vladimir Lizunov, Robert L. Wilson, Kevin J. Carpenter, Raehyun Kim, Ian D. Hutcheon, Joshua Zimmerberg, Peter K. Weber, and Mary L. Kraft. Direct chemical evidence for sphingolipid domains in the plasma membranes of fibroblasts. *Proceedings of the National Academy of Sciences*, 110(8):E613–E622, 2013.

[37] Eva Sevcsik, Mario Brameshuber, Martin Fölser, Julian Weghuber, Alf Honigmann, and Gerhard J. Schütz. Gpi-anchored proteins do not reside in ordered domains in the live cell plasma membrane. *Nat Commun.*, 6((6969)), April 2015.

[38] Ilya Levental, Kandice R. Levental, and Frederick A. Heberle. Lipid rafts: Controversies resolved, mysteries remain. *Trends in Cell Biology*, 30(5):341–353, 2020.

[39] Wikipedia contributors. Fluid mosaic model — Wikipedia, the free encyclopedia. `https://en.wikipedia.org/w/index.php?title=Fluid_mosaic_model&oldid=1041239169`, 2021.

[40] Wikipedia contributors. Lipid raft — Wikipedia, the free encyclopedia. `https://en.wikipedia.org/w/index.php?title=Lipid_raft&oldid=1043020984`, 2021.

[41] PG Saffman and M Delbrück. Brownian motion in biological membranes. *Proceedings of the National Academy of Sciences of the United States of America*, 72(8):3111—3113, August 1975.

[42] M. J. Boussinesq. Speed of the slow, uniform fall of a liquid spherical drop in a viscous fluid of lesser specific weight. *Ann. Chim. Phys. 29*, page 364–371, 1913.

[43] Byung Mook Weon and Jung Ho Je. Capillary force repels coffee-ring effect. *Phys. Rev. E*, 82:015305, Jul 2010.

[44] Jiayu Li and Harishankar Manikantan. Influence of interfacial rheology on viscous fingering. *Phys. Rev. Fluids*, 6:074001, Jul 2021.

[45] D. Regan, J. Williams, P. Borri, and W. Langbein. Lipid Bilayer Thickness Measured by Quantitative DIC Reveals Phase Transitions and Effects of Substrate Hydrophilicity. *Langmuir*, 35(43):13805–13814, 10 2019.

[46] L.E. Scriven. Dynamics of a fluid interface equation of motion for newtonian surface fluids. *Chemical Engineering Science*, 12(2):98–108, 1960.

[47] J. C. Slattery and L. Sagis. *Interfacial Transport Phenomena.* Springer, 2007.

[48] Harishankar Manikantan and Todd M. Squires. Surfactant dynamics: hidden variables controlling fluid flows. *Journal of Fluid Mechanics*, 892:P1, 2020.

[49] Thomas M. Fischer. Comment on "shear viscosity of langmuir monolayers in the low-density limit". *Phys. Rev. Lett.*, 92:139603, Apr 2004.

[50] Howard A. Stone and Hassan Masoud. Mobility of membrane-trapped particles. *Journal of Fluid Mechanics*, 781:494–505, 2015.

[51] C. Barentina, P. Muller, C. Yberta, J.-F. Joannyb, and J.-M. di Meglioc. Shear viscosity of polymer andsurfactant monolayers. *Eur. Phys. J. E*, 2:153–159, 2000.

[52] M. Sickert, F. Rondelez, and H. A. Stone. Single-particle brownian dynamics for characterizing the rheology of fluid langmuir monolayers. *EPL*, 79(6):66005, aug 2007.

[53] Ryan D. Booker and Amadeu K. Sum. Biophysical changes induced by xenon on phospholipid bilayers. *Biochimica et Biophysica Acta (BBA) - Biomembranes*, 1828(5):1347–1356, 2013.

[54] McIntosh TJ and Simon SA. Hydration force and bilayer deformation: a reevaluation. *Biochemistry*, 14:4058–66, 1986.

[55] Evan Evans and Erich Sackmann. Translational and rotational drag coefficients for a disk moving in a liquid membrane associated with a rigid substrate. *Journal of Fluid Mechanics*, 194:553–561, 1988.

[56] David K. Lubensky and Raymond E. Goldstein. Hydrodynamics of monolayer domains at the air–water interface. *Physics of Fluids*, 8(4):843–854, 1996.

[57] Alex J. Levine and F. C. MacKintosh. Dynamics of viscoelastic membranes. *Phys. Rev. E*, 66:061606, Dec 2002.

[58] Meisam Pourali, Nick O. Jaensson, and Martin Kröger. Drag on a spheroidal particle at clean and surfactant-laden interfaces: effects of particle aspect ratio, contact angle and surface viscosities. *Journal of Fluid Mechanics*, 924:A30, 2021.

[59] Goodrich. The theory of absolute surface shear viscosity.i. *Proc. R. Soc. Lond. A F. C.*, 1969.

[60] Zell ZA, Nowbahar A, Mansard V, Leal LG, Deshmukh SS, Mecca JM, Tucker CJ, and Squires TM. Surface shear inviscidity of soluble surfactants. *Proc Natl Acad Sci USA*, 111(10):3677–82, Mar 2014.

[61] Subhasish Dey, Sk Zeeshan Ali, and Ellora Padhi. Terminal fall velocity: the legacy of stokes from the perspective of fluvial hydraulics. *Proceedings of the Royal Society A: Mathematical, Physical and Engineering Sciences*, 475(2228):20190277, 2019.

[62] R. Peters and R. J. Cherry. Lateral and rotational diffusion of bacteriorhodopsin in lipid bilayers: Experimental test of the -delbruck equations. *Proceedings of the National Academy of Sciences*, 79(14):4317–4321, 1982.

[63] W. L. C. Vaz, D. Hallmann, R. M. Clegg, A. Gambacorta, and M. De Rosa. A comparison of the translational diffusion of a normal and a membrane-spanning lipid in Lα phase 1-palmitoyl-2-oleoylphosphatidylcholine bilayers. *European Biophysics Journal*, 12(1):19–24, April 1985.

[64] V. Prasad, S. A. Koehler, and Eric R. Weeks. Two-particle microrheology of quasi-2d viscous systems. *Phys. Rev. Lett.*, 97:176001, Oct 2006.

[65] Pietro Cicuta, Sarah L. Keller, and Sarah L. Veatch. Diffusion of liquid domains in lipid bilayer membranes. *The Journal of Physical Chemistry B*, 111(13):3328–3331, 2007. PMID: 17388499.

[66] Haim Diamant. Hydrodynamic interaction in confined geometries. *Journal of the Physical Society of Japan*, 78(4):041002, 2009.

[67] Naomi Oppenheimer and Haim Diamant. Correlated dynamics of inclusions in a supported membrane. *Phys. Rev. E*, 82:041912, Oct 2010.

[68] Howard A. Stone and Armand Ajdari. Hydrodynamics of particles embedded in a flat surfactant layer overlying a subphase of finite depth. *Journal of Fluid Mechanics*, 369:151–173, 1998.

[69] Steven Vandebril, Aly Franck, Gerald G. Fuller, Paula Moldenaers, and Jan Vermant. A double wall-ring geometry for interfacial shear rheometry. *Rheologica Acta*, 49:131–144, 2010.

[70] Carlton F. Brooks, Gerald G. Fuller, Curtis W. Frank, and Channing R. Robertson. An interfacial stress rheometer to study rheological transitions in monolayers at the air-water interface. *Langmuir*, 15(7):2450–2459, 1999.

[71] O. H Soo-Gun and John C. Slattery. Disk and biconical interfacial viscometers. *Journal of Colloid and Interface Science*, 67:516–525, 1978.

[72] R. S. Ghaskadvi and Michael Dennin. A two-dimensional couette viscometer for langmuir monolayers. *Review of Scientific Instruments*, 69(10):3568–3572, 1998.

[73] Reinhard Miller and L Liggieri. *Progress in Colloid and Interface Science. Vol. 1: Interfacial Rheology*. Leiden : Brill, 2009.

[74] L. Liggieri, V. Attolini, M. Ferrari, and F. Ravera. Measurement of the surface dilational viscoelasticity of adsorbed layers with a capillary pressure tensiometer. *J Colloid Interface Sci*, 255(2):225–235, Nov 2002.

[75] S.Q. Choi, S. Steltenkamp, J.A. Zasadzinski, and T.M. Squires. Active microrheology and simultaneous visualization of sheared phospholipid monolayers. *Nat Commun.*, 2(312), May 2011.

[76] Vladimir M. Kaganer, Helmuth Möhwald, and Pulak Dutta. Structure and phase transitions in langmuir monolayers. *Rev. Mod. Phys.*, 71:779–819, Apr 1999.

[77] KyuHan Kim, Siyoung Q. Choi, Joseph A. Zasadzinski, and Todd M. Squires. Interfacial microrheology of dppc monolayers at the air–water interface. *Soft Matter*, 7:7782–7789, 2011.

[78] Eline Hermans and Jan Vermant. Interfacial shear rheology of dppc under physiologically relevant conditions. *Soft Matter*, 10:175–186, 2014.

[79] Marcel Vrânceanu, Karin Winkler, Hermann Nirschl, and Gero Leneweit. Surface rheology of monolayers of phospholipids and cholesterol measured with axisymmetric drop shape analysis. *Colloids and Surfaces A: Physicochemical and Engineering Aspects*, 311(1):140–153, 2007. Engineering Particle Technology.

[80] C. Alonso and J. A. Zasadzinski. A brief review of the relationships between monolayer viscosity, phase behavior, surface pressure, and temperature using a simple monolayer viscometer. *J Phys Chem B*, 110(44):22185–22191, Nov 2006.

[81] Vladimir M. Kaganer, Helmuth Möhwald, and Pulak Dutta. Structure and phase transitions in langmuir monolayers. *Rev. Mod. Phys.*, 71:779–819, Apr 1999.

[82] Rachel E. Kurtz, Arno Lange, and Gerald G. Fuller. Interfacial rheology and structure of straight-chain and branched fatty alcohol mixtures. *Langmuir*, 22(12):5321–5327, 2006.

[83] Z. A. Zell, A. Nowbahar, V. Mansard, L. G. Leal, S. S. Deshmukh, J. M. Mecca, C. J. Tucker, and T. M. Squires. Surface shear inviscidity of soluble surfactants. *Proc Natl Acad Sci U S A*, 111(10):3677–3682, Mar 2014.

[84] Manikantan Harishankar and Squires Todd M. Irreversible particle motion in surfactant-laden interfaces due to pressure-dependent surface viscosity. *Proc. R. Soc. A.*, page 473:20170346, 2017.

[85] Harishankar Manikantan and Todd M. Squires. Pressure-dependent surface viscosity and its surprising consequences in interfacial lubrication flows. *Phys. Rev. Fluids*, 2:023301, Feb 2017.

[86] Hassan Masoud and Howard A. Stone. The reciprocal theorem in fluid dynamics and transport phenomena. *Journal of Fluid Mechanics*, 879:P1, 2019.

[87] Ramanathan Vishnampet and David Saintillan. Concentration instability of sedimenting spheres in a second-order fluid. *Physics of Fluids*, page 10.1063/1.4733700, 2012.

[88] Naomi Oppenheimer and H. Diamant. Correlated diffusion of membrane proteins and their effect on membrane viscosity. *Biophysical journal*, 96 8:3041–9, 2009.

[89] Naomi Oppenheimer, David B. Stein, and Michael J. Shelley. Rotating membrane inclusions crystallize through hydrodynamic and steric interactions. *Phys. Rev. Lett.*, 123:148101, Oct 2019.

[90] Bartosz A. Grzybowski, Howard A. Stone, and George M. Whitesides. Dynamic self-assembly of magnetized, millimetre-sized objects rotating at a liquid–air interface. *Nature*, 405(6790):1033–1036, Jun 2000.

[91] E. Wigner. On the interaction of electrons in metals. *Phys. Rev.*, 46:1002–1011, Dec 1934.

[92] Yusuke Goto and Hajime Tanaka. Purely hydrodynamic ordering of rotating disks at a finite reynolds number. *Nature Communications*, 6(1), 2015.

[93] Harishankar Manikantan. Tunable collective dynamics of active inclusions in viscous membranes. *Phys. Rev. Lett.*, 125:268101, Dec 2020.

[94] SeungHye Han and Rama K. Mallampalli. The role of surfactant in lung disease and host defense against pulmonary infections. *Annals of the American Thoracic Society*, 12(5):765–774, May 2015.

[95] Eline Hermans, M. Saad Bhamla, Peter Kao, Gerald G. Fuller, and Jan Vermant. Lung surfactants and different contributions to thin film stability. *Soft Matter*, 11:8048–8057, 2015.

[96] Kyongmin Yeo, Enkeleida Lushi, and Petia M. Vlahovska. Collective dynamics in a binary mixture of hydrodynamically coupled microrotors. *Physical Review Letters*, 114(18), 2015.

[97] Thorsten B. Blum, Alexander Hahn, Thomas Meier, Karen M. Davies, and Werner Kühlbrandt. Dimers of mitochondrial atp synthase induce membrane curvature and self-assemble into rows. *Proceedings of the National Academy of Sciences*, 116(10):4250–4255, 2019.

[98] Daichi Okuno, Ryota Iino, and Hiroyuki Noji. Rotation and structure of FoF1-ATP synthase. *The Journal of Biochemistry*, 149(6):655–664, 04 2011.

[99] Nathan E. Barlow, Guido Bolognesi, Stuart Haylock, Anthony J. Flemming, Nicholas J. Brooks, Laura M. C. Barter, and Oscar Ces. Rheological droplet interface bilayers (rheo-dibs): Probing the unstirred water layer effect on membrane permeability via spinning disk induced shear stress. *Scientific Reports*, 7(1), 2017.